Additive Manufacturing 55 (2022) 102887

Contents lists available at ScienceDirect

Additive Manufacturing

journal homepage: www.elsevier.com/locate/addma

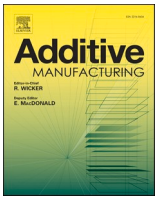

Research paper

Enhancing specific energy absorption of additively manufactured titanium lattice structures through simultaneous manipulation of architecture and constituent material

Jingqi Zhang [a,1], Yingang Liu [a,1], Behzad Bahrami Babamiri [b], Ying Zhou [c], Matthew Dargusch [a], Kavan Hazeli [d,*], Ming-Xing Zhang [a,*]

[a] School of Mechanical and Mining Engineering, The University of Queensland, St. Lucia, Brisbane, Queensland 4072, Australia
[b] Mechanical and Aerospace Engineering Department, University of Alabama in Huntsville, USA
[c] School of Mechanical, Medical and Process Engineering, Queensland University of Technology, Brisbane, Queensland 4001, Australia
[d] Aerospace and Mechanical Engineering Department, The University of Arizona, USA

ARTICLE INFO

Keywords:
Additive manufacturing
Laser powder bed fusion
Lattice structures
Titanium
Specific energy absorption
Finite element analysis

ABSTRACT

Titanium lattice structures have found a wide range of lightweight applications. However, lattice structures made from the commonly-used commercially pure titanium (CP−Ti) and Ti−6Al−4V exhibit either low strength or post-yielding softening/collapse under uniaxial compression, making them less attractive to energy absorbing applications. In the present work, a series of titanium gyroid lattice structures have been designed and additively manufactured by laser powder bed fusion (L-PBF) to enhance the specific energy absorption (SEA) through manipulation of the architecture and the constituent material. Experimental results show that tailoring the sheet thickness gradient of gyroid lattice structures enables the transformation of the macroscopic deformation mode from hardening followed by softening, which is commonly seen in lattice structures, to continuous hardening. The addition of MgO nanoparticles to CP−Ti feedstock further improves the yield strength through oxygen solute strengthening, while maintaining the continuous hardening behaviour without any post-yielding softening or collapse. As a result, when both sheet thickness gradient and MgO are introduced, the SEA of the uniform gyroid lattice structure is enhanced by approximately 63% due to the combination of continuous hardening behaviour and high strength. Finite element analysis based on the modified volumetric hardening model has been performed to shed light on the underlying mechanism that governs the continuous hardening behaviour. This study demonstrates the tremendous potential of marrying architecture engineering with material design to create high performance lightweight lattice structures by L-PBF.

1. Introduction

Lattice structures are highly desirable for a wide variety of applications, such as structural components, energy absorption, heat exchange, mass transport and tissue engineering [1–6]. With the advance of additive manufacturing (AM), geometrically complex lattice structures can be produced with well-controlled quality and high performance. Over the past decade, substantial efforts have been devoted to the design and fabrication of additively manufactured lattice structures, with the aim of improving the mechanical and functional properties to the best of their abilities. In the case of mechanical applications, maximizing the mechanical efficiency (in terms of mechanical performance per unit weight) has been a long-time pursuit of lightweight design [7–11]. It is well recognized that the mechanical performance of lattice structure is governed by the relative density, the architecture and the mechanical property of constituent material [7,11]. Generally, mechanical performance and light weighting are mutually exclusive in lattice structures. For example, the yield strength of lattice structure (σ_y) usually decreases with decreasing relative density, following the classical Gibson–Ashby relationship $\sigma_y/\sigma_{ys} \propto (\rho/\rho_s)^n$ (where σ_{ys} is the yield strength of the solid constituent material, $\bar{\rho} = \rho/\rho_s$is the relative density, ρ is the density of lattice structure, ρ_s is the density of the solid constituent material, and

* Corresponding authors.
E-mail addresses: hazeli@arizona.edu (K. Hazeli), mingxing.zhang@uq.edu.au (M.-X. Zhang).
[1] These authors contributed equally to this work.

https://doi.org/10.1016/j.addma.2022.102887
Received 26 February 2022; Received in revised form 3 May 2022; Accepted 9 May 2022
Available online 13 May 2022

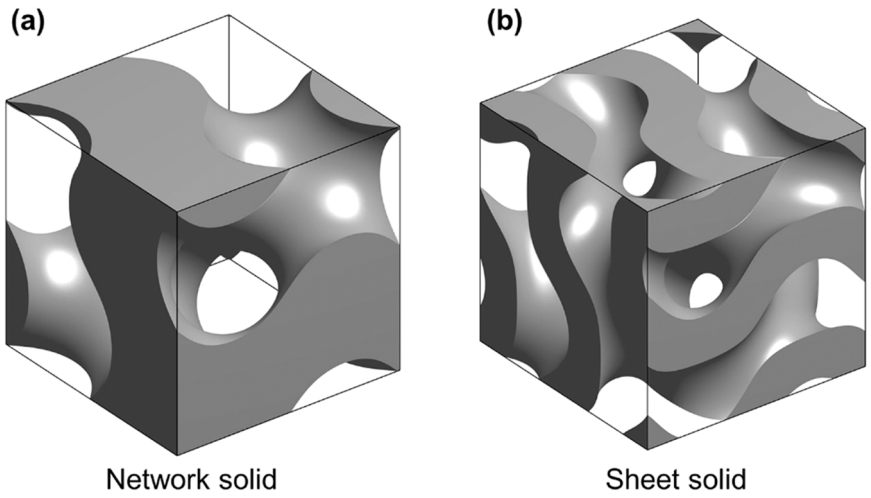

Fig. 1. (a) Network- and (b) sheet-based gyroid unit cell.

the exponent n depends on the architecture) [1,2]. Similarly, the energy absorption of lattice structure drops monotonically as the relative density decreases [12–14]. The trade-off between mechanical performance and lightweightness makes it challenging to create mechanically robust yet lightweight lattice structures for applications where high performance and minimal weight are the key design targets.

On the other hand, manipulation of the architecture and the constituent material of lattice structure offers more freedom to enhance the mechanical performance while minimizing the weight. For energy absorbing applications, it ideally requires that the lattice structure exhibits both high strength and a stress–strain curve with a stress plateau over a large strain range [1,15,16]. In the vast library of lattice structures, the gyroid triply periodic minimal surfaces (TPMS) have been attracting intensive interest, due to their exceptional high strength and energy absorbing capability [17–19]. In general, the gyroid TPMS can be divided into two types: network and sheet (Fig. 1). It has been demonstrated that the sheet-based gyroid TPMS are structurally stiffer than the network type [20]. However, the gyroid lattice structures, as well as many other types of lattice structures, typically show post-yielding softening or collapse when subjected to compressive loading [21]. This intrinsic mechanical behaviour has been reported in the gyroid lattice structures made from a wide variety of materials, spanning from polymers [22] to metallic materials (such as titanium alloy [23,24], steel [21] and aluminium alloy [25]). Such a mechanical response with softening or collapse is not desirable for energy absorption applications. Over the past few years, there have been a few studies on improving the energy absorption capability of gyroid lattice structures through functionally graded design. For example, Yang et al. [26] designed network-based gyroid lattice structures with sheet thickness gradient in one direction. Similarly, Li et al. [27] introduced the one-direction gradient into sheet-based gyroid lattice structures. However, it is found that such a design strategy has a limited contribution to the energy absorption improvement, because it cannot either eliminate the post-yielding softening/collapse or substantially enhance the strength. Alternatively, radially graded gyroid lattice structures are introduced [28]. It has been shown that the yield strength can be improved through the radial design while the post-yielding collapse remains. In contrast, a design approach that can simultaneously achieve high strength and eliminate the post-yielding softening/collapse would realize lattice structures with outstanding energy absorbing capability.

In addition to the architecture, the constituent material has a significant impact on the mechanical performance of lattice structures. Titanium and titanium alloys, typically CP−Ti and Ti−6Al−4V, stand out among the commonly used metallic materials (such as steels and aluminium alloys) in a broad range of applications, primarily due to their high specific strength (the strength-to-weight ratio) and excellent corrosion resistance. Like their bulk materials, CP−Ti and Ti−6Al−4V, when architected into lattice structures, perform distinctly under uniaxial compression. The lattice structure made from CP−Ti typically exhibits relatively low strength but can continuously accommodate high strains without collapse [17], In contrast, Ti−6Al−4V lattice structure is relatively strong; however, it undergoes progressive crushing after yielding, thereby giving rise to oscillations in the stress–strain curve [29]. In both cases, the low strength and the post-yielding softening/collapse make CP−Ti and Ti−6Al−4V less attractive for energy absorption applications.

Over the past decades, in-situ alloying has been commonly practiced in the development of new titanium alloys for AM [30], but this approach has seen limited success in the fabrication of titanium lattice structures. Among the alloying elements of titanium, the β-isomorphous stabilizers (such as Mo, Nb and Ta) are essential for high-strength β titanium alloys. However, owing to the high melting point, in-situ alloying CP−Ti with these elements often leads to elemental segregation and/or unmelted particles in the as-fabricated lattice structures [31], especially when the additive powders with a large size and/or a high addition level are used. This, inevitably, adds challenges to achieve uniform and reproducible mechanical properties. Alternatively, the β-eutectoid stabilizers (such as Cu, Ni and Fe) possess comparable melting points to titanium and much higher diffusion coefficients in titanium than the β-isomorphous type. However, these elements can dramatically embrittle the lattice structure due to the formation of intermetallic compounds [32]. Within the limited commonly used α stabilizers, nitrogen (N) and oxygen (O) are known to have a strong solid solution strengthening effect in titanium. These naturally abundant and cost-effective elements, if controllably used as the additive, may facilitate the development of titanium lattice structures with exceptional mechanical performance. Despite the concept of in-situ gas-based alloying having been demonstrated in additively manufactured bulk titanium alloys [33], it remains challenging to extend this strategy to fabricate lattice structures in a controllable manner, given the highly dynamic reaction of the N_2 or O_2 atmosphere with titanium feedstock under laser exposure.

The aim of this study is to enhance the specific energy absorption (SEA) of sheet-based gyroid lattice structures through manipulation of both architecture and constituent material. To this end, sheet-based gyroid lattice structures with uniform and graded sheet thickness at the same relative density were first designed and fabricated from the CP−Ti feedstock, with the aim of addressing the post-yielding softening behaviour. Then, MgO nanoparticles were introduced to CP−Ti powders as a source of oxygen solute strengthening to further tailor the mechanical properties. The initial selection of MgO nanoparticle was based upon the up-front mechanical mixing experiments, which indicated a

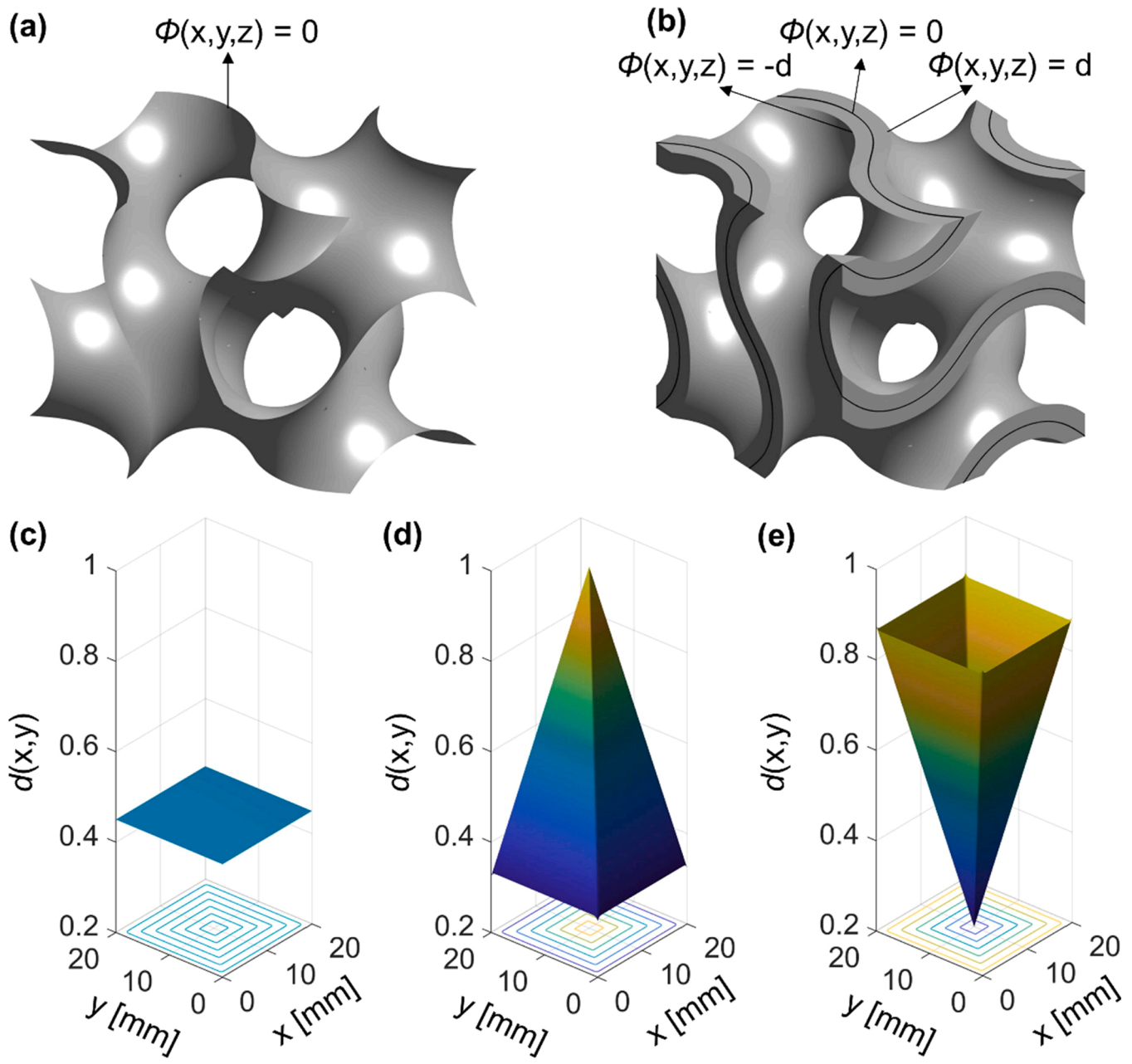

Fig. 2. (a) Sheet-based gyroid TPMS, (b) sheet-based gyroid unit cell, and (c-e) higher dimensional level-set function *d(x,y)* for (c) uniform lattice structure, (d) I2O lattice structure and (e) O2I lattice structure, along with their corresponding projected thickness distribution in the *xy*-plane.

homogeneous distribution of MgO nanoparticles in the titanium matrix powders, in contrast to apparent agglomerations of other oxides such as ZnO, TiO_2 and ZrO_2.

The structure of this article is organized as follows. Different types of lattice structures are first designed in Section 2 and are then additively manufactured as described in Section 3. The lattice samples are morphologically and microstructurally characterized in Section 4.1. In Section 4.2, the samples are mechanically tested in compression. The obtained compressive stress–strain curves are used to determine the SEA of lattice structures in Section 4.3. Finally, finite element analysis (FEA) is carried out to shed light on the underlying deformation mechanisms in Section 4.4.

2. Design of gyroid lattice structures

The sheet-based gyroid lattice structures were designed in accordance with ISO 13314:2011 standard [34]. The sheet-based gyroid TPMS can be mathematically formulated by a level-set function $\Phi(x,y,z)$, which is given by [19]:

$$\Phi\left(x,y,z\right) = \cos\left(\frac{2\pi}{a}\cdot x\right)\sin\left(\frac{2\pi}{a}\cdot y\right) + \cos\left(\frac{2\pi}{a}\cdot y\right)\sin\left(\frac{2\pi}{a}\cdot z\right) + \cos\left(\frac{2\pi}{a}\cdot z\right)\sin\left(\frac{2\pi}{a}\cdot x\right) \quad (1)$$

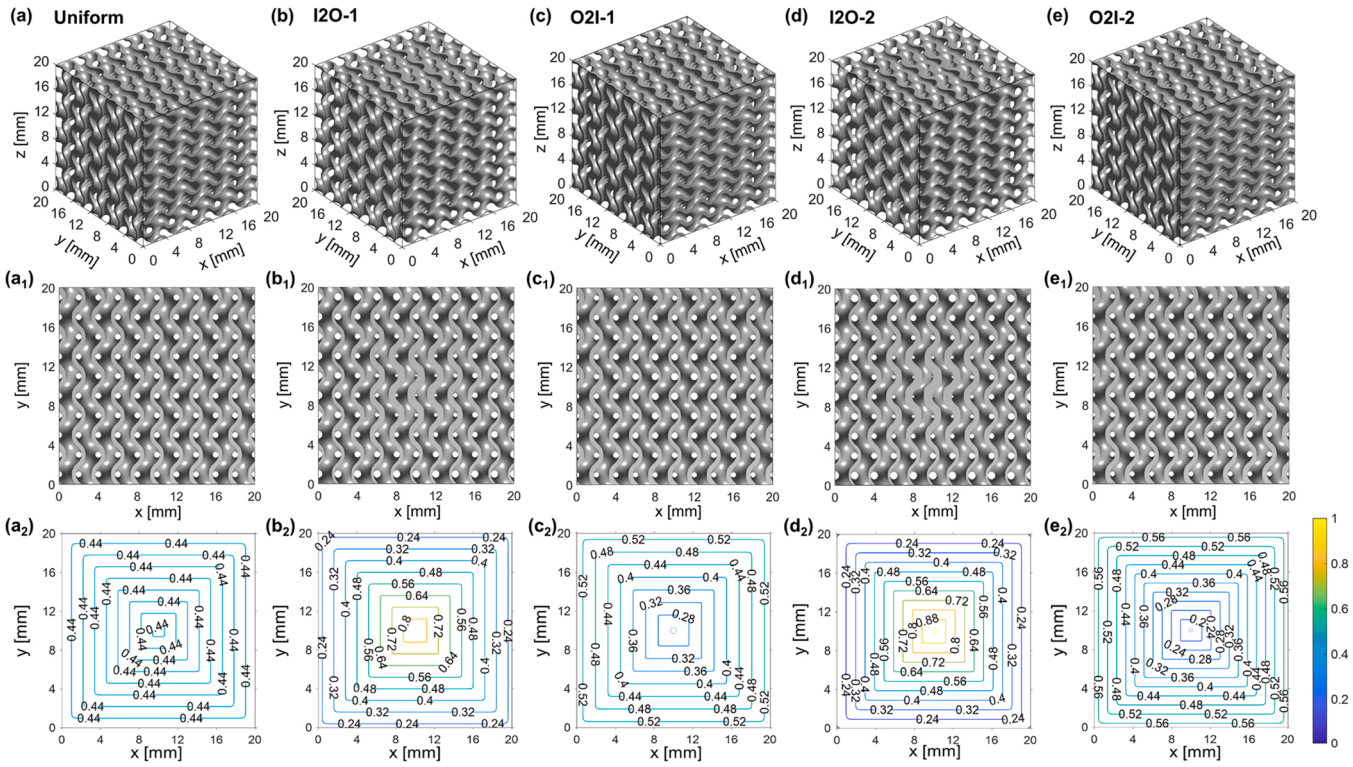

Fig. 3. Five different types of gyroid lattice structures used in this study. (a-e) the designed uniform, I2O-1, O2I-1, I2O-2 and O2I-2 lattice structures, (a_1-e_1) the upper surface of each type of lattice structure, and (a_2-e_2) the thickness distributions in terms of LSF d(x,y) of each type of lattice structure.

Table 1
The designed five gyroid lattice structures with different gradient ratios.

Type	Sign	α	β	n	l	w	$d\,(0,y_c)$	$d\,(x_c,y_c)$	Gradient ratio
Uniform	N.A.	N.A.	N.A.	50	N.A.	N.A.	0.4365	0.4365	1.00
I2O-1	+	1.00	-0.12	50	15	15	0.2133	0.8800	4.13
O2I-1	−	0.46	1.50	50	15	15	0.5390	0.2310	0.43
I2O-2	+	0.98	0	50	12	12	0.1633	0.9800	6.00
O2I-2	−	0.51	1.30	50	12	12	0.5780	0.1530	0.26

where a refers to the dimension of unit cell. The sheet-based gyroid TPMS (Fig. 2a) are defined as the zero-isosurface of Φ, (i.e., $\Phi(x,y,z) = 0$), while the gyroid unit cell (Fig. 2b) is the enclosed domain between two isosurfaces $\Phi(x,y,z) = d$ and $\Phi(x,y,z) = -d$, where the value of d defines the sheet thickness.

The gyroid lattice structure is an assembly of repetitive unit cells along coordinate axes. In the case of uniform sheet thickness, d is a constant value. The uniform gyroid lattice structure is therefore created by arranging identical unit cells along x-, y- and z-directions. While for the graded sheet thickness, d is defined as a function. In this work, gyroid lattice structures with graded sheet thickness in the xy-plane were designed by specifying d as a function given by:

$$d(x,y) = \alpha \cdot [\beta \pm \varphi(x,y)] \tag{2}$$

where $\varphi(x, y)$ is the level-set function of a superellipse centred at (x_c, y_c), which is defined as:

$$\varphi\left(x,y\right) = 1 - \left(\left|\frac{x-x_c}{l}\right|^n + \left|\frac{y-y_c}{w}\right|^n\right)^{1/n} \tag{3}$$

The degree of sheet thickness gradient can be controlled by tuning the values of α, β, n, l, and w. Fig. 2 depicts the higher-dimensional level-set function $d(x,y)$and its projected thickness distribution in the xy-plane for both uniform (Fig. 2c) and graded lattice structures (Figs. 2d and 2e). With Eqs. (2) and (3), two types of gyroid lattice structures with graded sheet thickness can be defined by specifying the sign " + " or " − ", namely, the inner-to-outer (I2O) and the outer-to-inner (O2I).

As shown in Fig. 3a-e, one uniform (Fig. 3a) and four graded gyroid lattice structures (Fig. 3b-e) have been constructed using MATLAB software in a cuboid design domain with dimension of 20 mm × 20 mm × 20 mm. Each lattice structure contains 5 × 5 × 5 unit cells and each unit cell has a dimension of 4 mm × 4 mm × 4 mm. The total volume of each lattice structure (i.e., the relative density) is kept fixed as 27%. The values of parameters in Eqs. (2) and (3) are listed in Table 1. The selection of these values is based on the criterion that keeps the design relative density of all lattice structures constant as 27% and the AM machine's capacity to create the minimum feature size (140 μm in this work). The upper surfaces and sheet thickness gradient of lattice structures are shown in Fig. 3a_1-e_1 and Fig. 3a_2-e_2, respectively. The degree of sheet thickness gradient of four graded gyroid lattice structures is represented in terms of the gradient ratio, which is defined by $d(x_c,y_c)/d(0,y_c)$. It is evident that the gradient ratio is larger than 1 for the I2O designs whereas smaller than 1 for the O2I designs (Table 1).

3. Experimental and simulation procedures

The plasma-atomized CP−Ti powders used in this work were supplied by AP&C Advanced Powders and Coatings Inc., with a particle size range of 20−63 μm. To select the most proper oxide as the trace

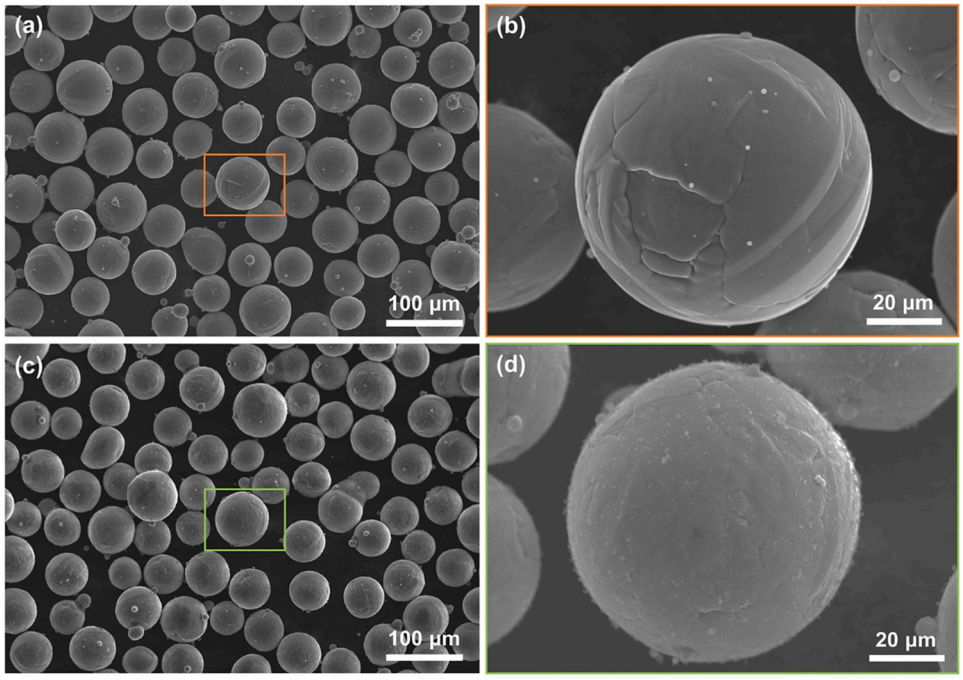

Fig. 4. Feedstocks for the fabrication of lattice structures: (a) CP−Ti powders, and (b) high magnification of individual CP−Ti powder in (a); (c) MgO-doped CP−Ti powders and (d) high magnification of individual MgO-coated CP−Ti powder in (c).

Table 2
The chemical compositions of CP−Ti samples without and with MgO addition (in wt%).

Material	Fe	O	N	H	Ti
CP-Ti	0.06	0.09	0.018	0.005	balance
MgO-doped CP-Ti	0.08	0.28	0.020	0.006	balance

additive, MgO (~30 nm), ZnO (~30 nm), TiO_2 (~25 nm) and ZrO_2 (3 mol% Y_2O_3 stabilized, 30−60 nm) nanoparticles with the addition level of 0.5 wt% were separately mixed with CP−Ti powders (50 g for each additive) using a Tubular shaker mixer for one hour. It was found that the MgO-doped and ZrO_2-doped powder mixtures did not show any dramatic agglomerations (Supplementary Fig. S1). Given a larger particle size and a higher density of ZrO_2, MgO nanoparticles were finally selected as the trace additive, which showed a fairly homogeneous distribution in the titanium feedstock (Fig. 4), as characterized by using a Hitachi SU3500 scanning electron microscope (SEM).

The gyroid lattice structures comprising a 5 × 5 × 5 array of unit cells with the total size of 20 mm × 20 mm × 20 mm were fabricated using an SLM®125HL machine (SLM Solutions GmbH, Germany), with a maximum output power of 400 W and a fibre laser wavelength of 1060 nm. Laser melting started when the oxygen level was reduced below 0.01 vol%. All lattice structures were built on support structures

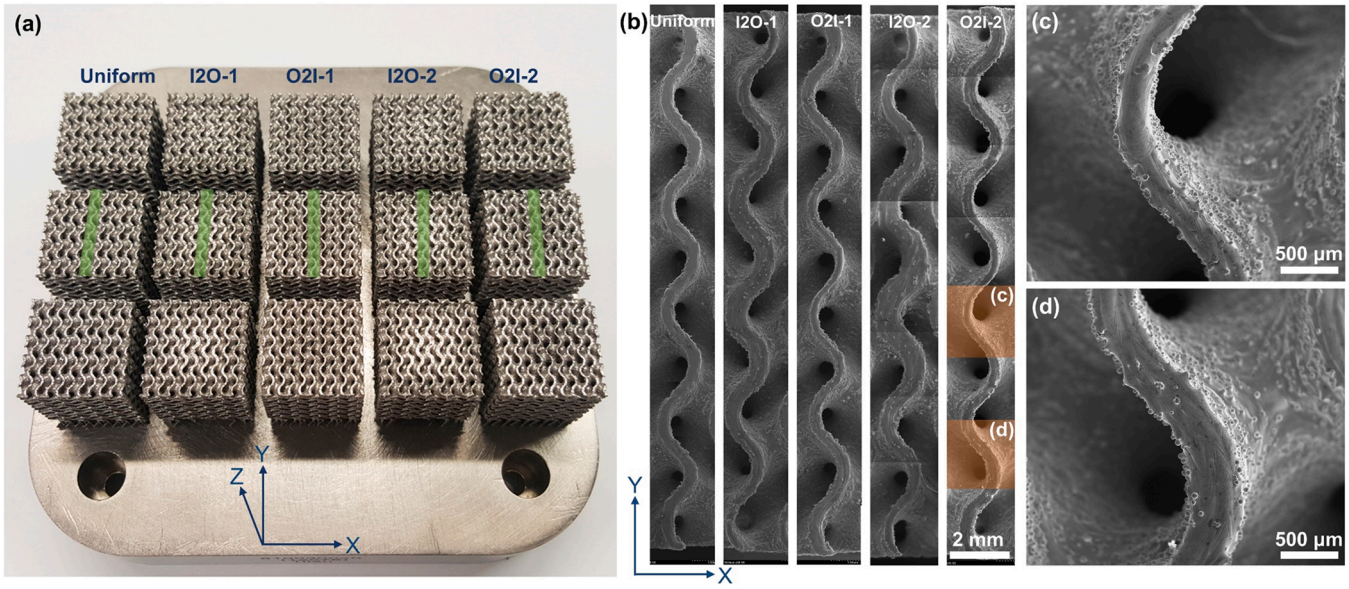

Fig. 5. (a) Macrographs of the as-fabricated gyroid lattice structures, (b) SEM images of the central region (in green colour) in the lattice structures in (a), (c) and (d) SEM images of the O2I-2 lattice structure at higher magnification.

Table 3
The relative porosity and mechanical properties of gyroid lattice structures.

Lattice type	Average relative density [%]	Yield strength [MPa]	Specific energy absorption [J/g]
Uniform	35.52	79.73 ± 2.7	17.5 ± 2.3
I2O-1	36.81	83.35 ± 2.1	21.3 ± 1.7
O2I-1	35.63	79.39 ± 3.4	19.4 ± 3.2
I2O-2	36.28	84.09 ± 2.9	23.3 ± 2.9
O2I-2	35.49	79.56 ± 3.3	20.3 ± 3.0
Uniform-MgO	36.45	95.82 ± 2.5	24.7 ± 2.4
I2O-1-MgO	36.31	102.5 ± 3.7	27.3 ± 2.7
O2I-1-MgO	35.98	102.47 ± 2.2	25.0 ± 3.4
I2O-2-MgO	36.58	111.16 ± 4.3	28.5 ± 3.1
O2I-2-MgO	35.99	91.04 ± 3.7	24.6 ± 3.4

(3 mm in height) using a "meander" scanning strategy. The lattice structures without and with MgO addition were fabricated using the same processing parameters, i.e., laser power of 350 W, layer thickness of 30 μm, hatch spacing of 120 μm and scanning speed of 1400 mm/s. The lattice samples were then removed from the substrate plate, followed by ultrasonic cleaning to remove the loosely adhered powders.

To obtain data that is required for FEA, both tensile and compressive properties of bulk CP−Ti are experimentally determined. Thus, CP−Ti solid parts with dimension of 40 mm (length) × 10 mm (width) × 40 mm (height) were produced using the aforementioned processing parameters. Cylindrical specimens (8 mm in diameter and 12 mm in height) and dog-bone-shaped tensile specimens with a gauge geometry of 10 mm (length) × 2.5 mm (width) × 2 mm (thickness) were machined from the bulk CP−Ti parts using the electrical discharge machining.

The relative density of all lattice structures was measured using the Archimedes' method. Selected lattice samples were characterized using a microfocus computed tomography (Micro-CT) system diondo d2 with a scanning solution of 4 μm. The structural morphology of lattice structures was characterized using a Hitachi SU3500 SEM. For electron backscatter diffraction (EBSD) characterization, the samples were ground and mechanically polished using a Struers OP-S suspension containing 20% of H_2O_2 for 30 min. EBSD characterization was performed using a JEOL JSM-7800 F SEM with a step size of 0.3 μm. The EBSD data was analysed using OIM Analysis 7.3 software. The chemical compositions of lattice structures without and with MgO addition were determined by using inductively coupled plasma atomic emission spectroscopy (ICP-AES) for metallic elements and by using LECO combustion analysis for non-metallic elements, as listed in Table 2.

Uniaxial compression tests were carried out on an Instron 5584 electromechanical universal testing machine at a constant strain rate of 0.001 s^{-1} for both lattice and bulk specimens. In the case of lattice structures, an overview of the experimental setup is provided in Supplementary Fig. S2. Two white dots were marked on the loading platens and the movement of these two dots during testing was tracked by an Instron AVE2 non-contacting video extensometer with a resolution of 0.5 μm. A video camera was also used to capture the dynamic deformation of lattice structures under the applied loading. At least three samples from each group were tested to confirm the reproductivity of mechanical properties. The compression testing was performed according to ISO 13314:2011 standard [34]. The compressive stress was calculated based on the compressive force divided by the initial cross-sectional area perpendicular to the loading direction. The compressive and tensile tests of bulk CP−Ti were performed according to ASTM E9–19 and ASTM E8/E8M-11 standards, respectively. The yield strength was determined using the 0.2% offset method.

Finite element simulations were performed on the uniform, I2O-2 and O2I-2 lattice structures made from CP−Ti using a 3D finite element method with an explicit algorithm that was established in the commercial software package ABAQUS. The models meshed with 4-node linear tetrahedral elements (C3D4) with a global size of 0.15 mm. Moreover, moving and fixed rigid plates were defined at the top and bottom of the lattice structure model, respectively, as demonstrated in Supplementary Fig. S3. The frictional contact coefficient between the rigid plates and the lattice structures was set to be 0.2. A

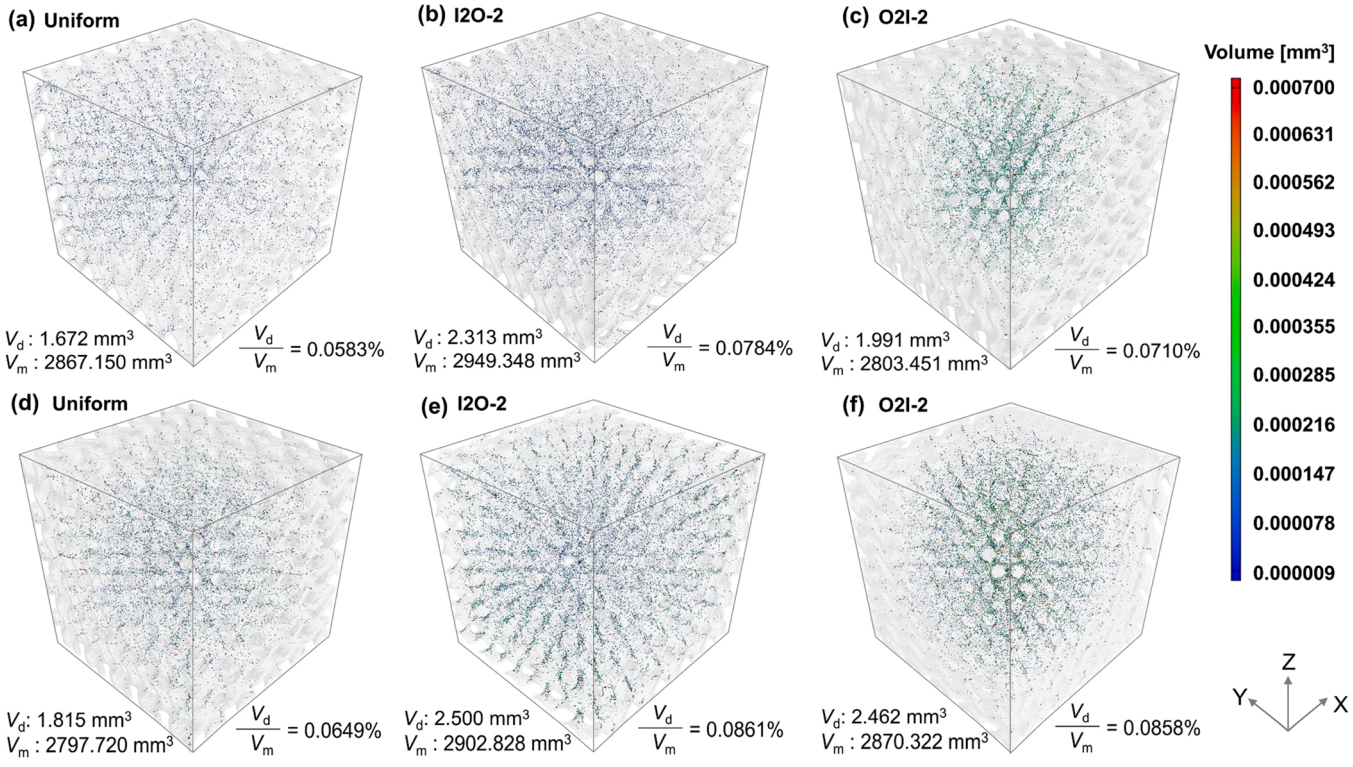

Fig. 6. Micro-CT characterization of different types of lattice structures without (a, b and c) and with (d, e and f) MgO addition.

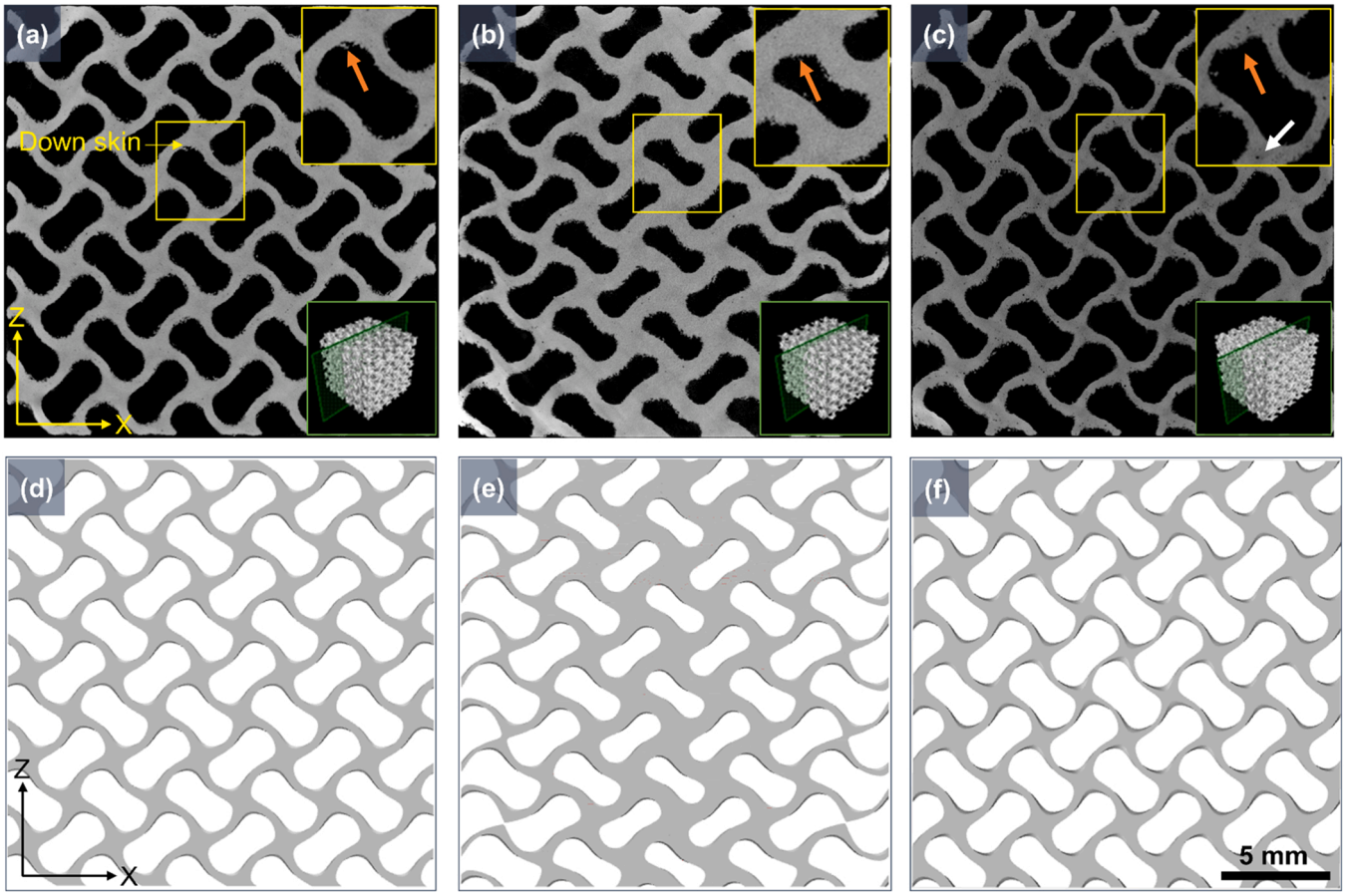

Fig. 7. Comparison of the Micro-CT characterization and the design model of uniform (a and d), I2O-2 (b and e) and O2I-2 (c and f) MgO-doped CP−Ti lattice structures in the XZ-plane. (a-c) Micro-CT images. The top-right insert shows higher magnification of the selected region marked with the yellow box. The bottom-right insert indicates where the Micro-CT image was taken. (d-f) the design model.

general contact algorithm was applied to the model to account for the contact between the struts during deformation. Loading was prescribed by applying a total displacement of 8 mm to the rigid moving plate at a constant strain rate of 0.1 s^{-1}. The ductile damage initiation and evolution criteria were implemented to predict the onset of damage. The damage initiation criterion used in this work is based on the Johnson-Cook damage model defined in [35]. More details of this method can be found in [36].

4. Results and discussion

4.1. Morphological and microstructural characterizations

The as-fabricated gyroid lattice structures with uniform and graded sheet thickness are shown in Fig. 5a. Higher magnification of lattice structures by SEM is presented in Fig. 5b, which shows the notable structural difference (the variation of sheet thickness) between the uniform, I2O and O2I lattice structures. It is evident that the uniform lattice structures display the constant sheet thickness whereas the graded types show the smooth, continuous sheet thickness variation from the outer to inner region. Additionally, apparent powder attachment is observed in the lattice structure (Figs. 5c and 5d), which leads to a higher measured relative density (35.49%−36.81%) than the targeted value (27%), as listed in Table 3. Selected samples without and with MgO addition (i.e., uniform, I2O-2 and O2I-2) are further characterized using Micro-CT in terms of the volume of defects (V_d), the volume of materials (V_m) and their ratio (V_d/V_m), as shown in Fig. 6. Generally, in both CP−Ti and MgO-doped CP−Ti lattice structures, engineering the architecture from uniform to graded results in a slight increase in both V_d and V_d/V_m. Besides, in the case of O2I-2 design, manufacturing defects are mainly distributed in the inner region of lattice structures (Figs. 6c and 6f). This suggests that the sheet thickness in this region is approaching to the limit of the AM machine's capability (i.e., 140 μm). On the other hand, introducing MgO to CP−Ti does not lead to a significant increase in manufacturing defects. For both uniform and I2O-2 lattice structures, V_d and V_d/V_m increase by less than 0.2 mm^3 and 0.01%, respectively, due to the MgO addition. The O2I-2 type shows a relatively apparent increase in V_d compared with the uniform and I2O-2 types. Nevertheless, the corresponding V_d/V_m is still kept at a low value (0.0858%), indicating a good manufacturing quality of lattice structures.

The dimensional accuracy of lattice structures is also investigated by comparing the Micro-CT image with its design model in the XZ-plane of MgO-doped CP−Ti lattice structures. In the case of uniform lattice structure (Figs. 7a and 7d), the geometry of pore is relatively well-controlled. Some loosely adhered powders (marked with the orange arrow in Fig. 7a) are still visible in the down skin of the lattice structure after the ultrasonic cleaning. While in the I2O-2 lattice structure (Figs. 7b and 7e), noticeable extra part can be found in the down skin region (marked with the orange arrow in Fig. 7b), causing mismatch between the as-built part and the design model. Such a mismatch can be also observed in O2I-2 lattice structure (Figs. 7c and 7f). Additionally, manufacturing defects is visible in the structure (marked with the white arrow in Fig. 7c). The loosely adhered powders and extra fused parts are important factors for a higher relative density compared with the design model.

It has been documented that the laser reflectivity of CP−Ti at the laser wavelength of 1060 nm is around 30% [37], whereas that of MgO

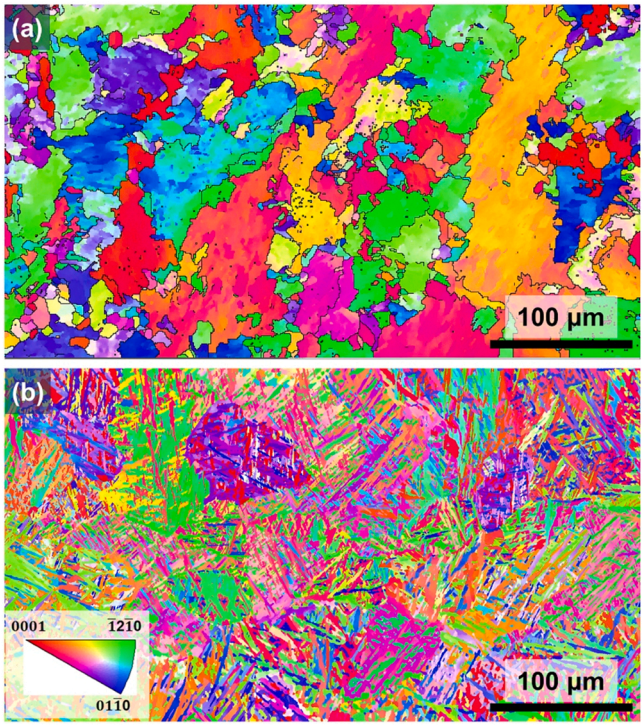

Fig. 8. EBSD IPF of the uniform structure made from (a) CP−Ti and (b) MgO-doped CP−Ti feedstocks.

is around 95% over a large laser wavelength range of 400 to 800 nm [38]. Despite an expected higher laser reflectivity of MgO than CP−Ti at the laser wavelength of 1060 nm, the addition of MgO to CP−Ti does not significantly produce more manufacturing defects in the lattice structures (Fig. 6). This is in contrast to the use of β-isomorphous and β-eutectoid stabilizers as the additive materials [31,32,39], which often results in either unmelted particles or unfavourable phases in the lattice structures and in turn may dramatically affect the macroscopic mechanical properties.

The microstructures of CP−Ti and MgO-doped CP−Ti lattice structures were characterized by EBSD (Fig. 8), which was performed in the central region of the uniform lattice structures. It can be observed from the EBSD inverse pole figures (IPF) that CP−Ti shows α grains with irregular shapes (Fig. 8a). In contrast, the addition MgO to CP−Ti produces α′ martensite with the acicular morphology (Fig. 8b). Since no Mg was detected by ICP-OPS (Table 2), the morphology change is attributed to the presence of oxygen, which is known to increase the martensitic transformation temperature, thereby promoting the formation of α′ martensite [40].

MgO possesses a very high melting point (2852 °C) and is known as one of the most stable oxides. According to the Ellingham diagram [41,42] in Fig. 9, the $2Mg + O_2 = 2MgO$ line lies below those of the common oxides (such as Al_2O_3 and TiO_2) over a wide temperature range, indicating a relatively high stability at these temperatures. However, the $2Mg + O_2 = 2MgO$ line slopes upwards more sharply at temperatures above 1100 °C and is expected to cut across the line for $Ti + O_2 = TiO_2$ at around 2100 °C. During L-PBF, it has been shown both numerically and experimentally [43,44] that the melt pool temperature of titanium or titanium alloy can reach higher than 2200 °C, at which the $2Mg + O_2 = 2MgO$ line lies above the $Ti + O_2 = TiO_2$ line. This implies that metallic Ti could reduce MgO to metallic Mg at such high temperatures. Because of a low boiling point (1091 °C), metallic Mg might vaporize during L-PBF. This may explain why Mg was no detected in this work. Indirect evidence to support this hypothesis is the reaction between Al and MgO. It has been well recognized that metallic Mg can reduce Al_2O_3 at relatively low temperatures such as during mechanical alloying [45], because Mg is more reactive than Al and the $2Mg + O_2 = 2MgO$ line lies below the $4/3Al + O_2 = 2/3Al_2O_3$ in the Ellingham diagram (Fig. 9). However, it has been shown by experiment that metallic Al can reduce MgO through the reaction $4MgO(s) + 2Al(l) = MgAl_2O_4(s) + 3Mg(g)$ at elevated temperatures (here, s, l and g represent solid, liquid and gas, respectively) [46]. Furthermore, if the reaction between Ti and MgO occurred during L-PBF, then titanium oxide(s) would be one of the reaction products. Given the very high temperature of melt pool, the product titanium oxide(s) would be readily fused due to the relatively low melting point(s). Besides, it is well known that oxygen has a high solubility in Ti. Therefore, the oxygen that was initially introduced through MgO addition is expected to fully dissolve in Ti, thus leading to the change in the morphology of microstructure, as shown in Fig. 8. However, further study is needed to provide direct evidence for the reaction between Ti and MgO during L-PBF.

4.2. Mechanical properties

Uniaxial compressive tests were performed to evaluate the effect of architecture engineering and material design on mechanical properties. Fig. 10 shows the typical force–displacement curves and the corresponding compressive stress–strain curves of five different lattice structures made from CP−Ti and MgO-doped CP−Ti feedstocks. Statistical values for the yield strength are also listed in Table 3. In general, the compressive stress–strain curves (Fig. 10d-f) and its force–displacement curves (Fig. 10a-c) exhibit an essentially similar behaviour. It can be seen from Fig. 10d that the uniform lattice structure displays the typical stages of compressive deformation as reported in the literature: (1) initial elastic region, (2) yielding, (3) post-yielding softening, and (4) densification [1]. The mechanical responses of two O2I lattice structures to the compressive loading follow a similar trend regardless of the change of sheet thickness gradient. In both uniform and O2I lattice structures, the post-yielding softening occurs in the compressive strain range of 20%− 30%. In contrast to the uniform and O2I lattice structures, the I2O designs show a continuous hardening behaviour after yielding. Despite the limited increase in the yield strength (Table 3), increasing the sheet thickness gradient from I2O-1 to I2O-2 significantly improves the compressive stress beyond yielding.

The addition of MgO to CP−Ti leads to substantial enhancement of yield strength but does not impact the strain hardening behaviour (Fig. 10e). As shown in Table 3, the yield strength increases by ~20% for the uniform lattice structure and by ~32% for the I2O-2 design when MgO is introduced. Additionally, two I2O lattice structures with different sheet thickness gradients (i.e., I2O-1-MgO and I2O-2-MgO) exhibit the continuous hardening behaviour, rather than the post-yielding softening which has been observed in the uniform and O2I designs. This suggests that such a continuous hardening behaviour originates intrinsically from the architecture and modifying the chemical composition through adding 0.5 wt% MgO does not change this intrinsic deformation behaviour of lattice structures. Fig. 10f compares the compressive stress−strain curves of the uniform and I2O-2 lattice structures without and with the addition of MgO. It is apparent that combining architecture engineering and material design not only enables elimination of the post-yielding softening, but also significantly increases the strength. The combination of the continuous hardening behaviour and high strength of I2O-2-MgO lattice structure indicates an exceptional energy absorption capability, as will be presented in the next section.

4.3. Specific energy absorption

The specific energy absorption (SEA) of lattice structures is generally defined as the energy absorbed per unit mass when the strain level reaches up to 0.3 under compressive loading, which is given by [12–14]:

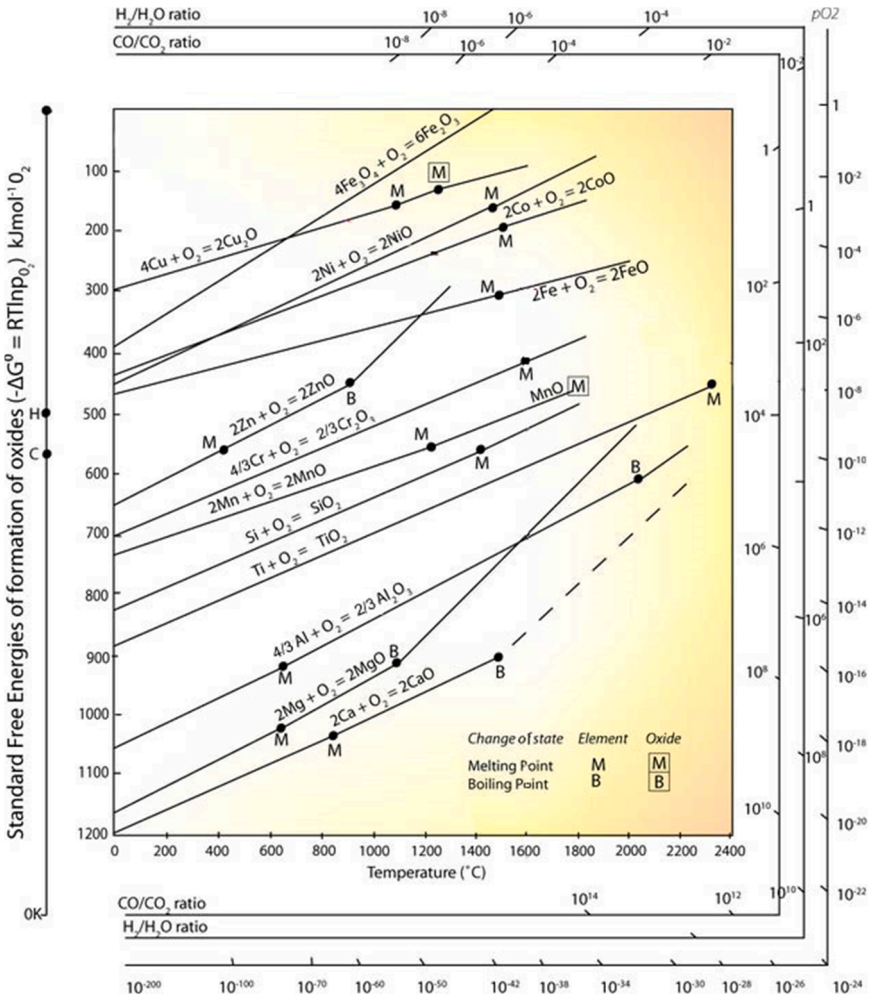

Fig. 9. Ellingham diagram [39,40].

$$\psi = \frac{1}{\rho}\int_0^{0.3} \sigma(\varepsilon)d\varepsilon \tag{4}$$

where ρ is the density of lattice structure. Eq. (4) can be rewritten as:

$$\psi = \frac{1}{\rho_s \cdot \frac{\rho}{\rho_s}}\int_0^{0.3} \sigma(\varepsilon)d\varepsilon \tag{5}$$

Since the relative density of lattice structures is defined as $\overline{\rho} = \rho/\rho_s$, the SEA of lattice structures can be determined by:

$$\psi = \frac{1}{\rho_s \overline{\rho}}\int_0^{0.3} \sigma(\varepsilon)d\varepsilon \tag{6}$$

The SEA was calculated from compressive stress–strain curves using a MATLAB code and is listed in Table 3. It is found that, when both sheet thickness gradient (I2O) and MgO are introduced, the SEA of lattice structures is enhanced by 63% from 17.5 ± 2.3 J/g (uniform) to 28.5 ± 3.1 J/g (I2O-2-MgO). To demonstrate the mechanical benefits from architecture engineering and material design, the SEA of gyroid lattice structures is compared with those of lattice structures made from various materials, as shown in Fig. 11. Overall, the I2O-2-MgO lattice structure shows outstanding SEA which markedly outperforms those made from 316 L stainless steel [13,14,47], aluminium alloys (such as 6061 alloy [48], AlSi10Mg [49,50] and Al-12Si [51]), titanium alloys (for example, Ti−6Al−4V [52,53] and Ti−6Al−4V + Mo [39]), polylactic acid [54], liquid photopolymer resin [55] and short-fibre reinforced nylon [56]. In particular, the SEA of I2O-2-MgO lattice structure is more than 1.5 times of the highest SEA of Ti− 6Al− 4V lattice structures with a close relative density. Such an exceptional SEA makes the I2O-2-MgO lattice structure highly attractive to applications where high strength, lightweightness and energy absorption are simultaneously required.

4.4. Finite element analysis

The continuous hardening behaviour of the I2O lattice structures is critical for the enhanced energy absorption capacity and does not vanish with the addition of 0.5 wt% MgO nanoparticles. In order to understand the mechanisms behind such an exceptional behaviour, FEA was performed on the selected lattice structures made from CP−Ti, i.e., the uniform, I2O-2 and O2I-2. The design models were used for FEA, because Micro-CT models led to a dramatic increase in the computational time.

The volumetric hardening model (VHM), which was originally proposed by Deshpande and Fleck [57], is very useful for the analysis of energy absorption lattice structures. However, this model assumes that the material exhibits the same behaviour in compression and tension. In

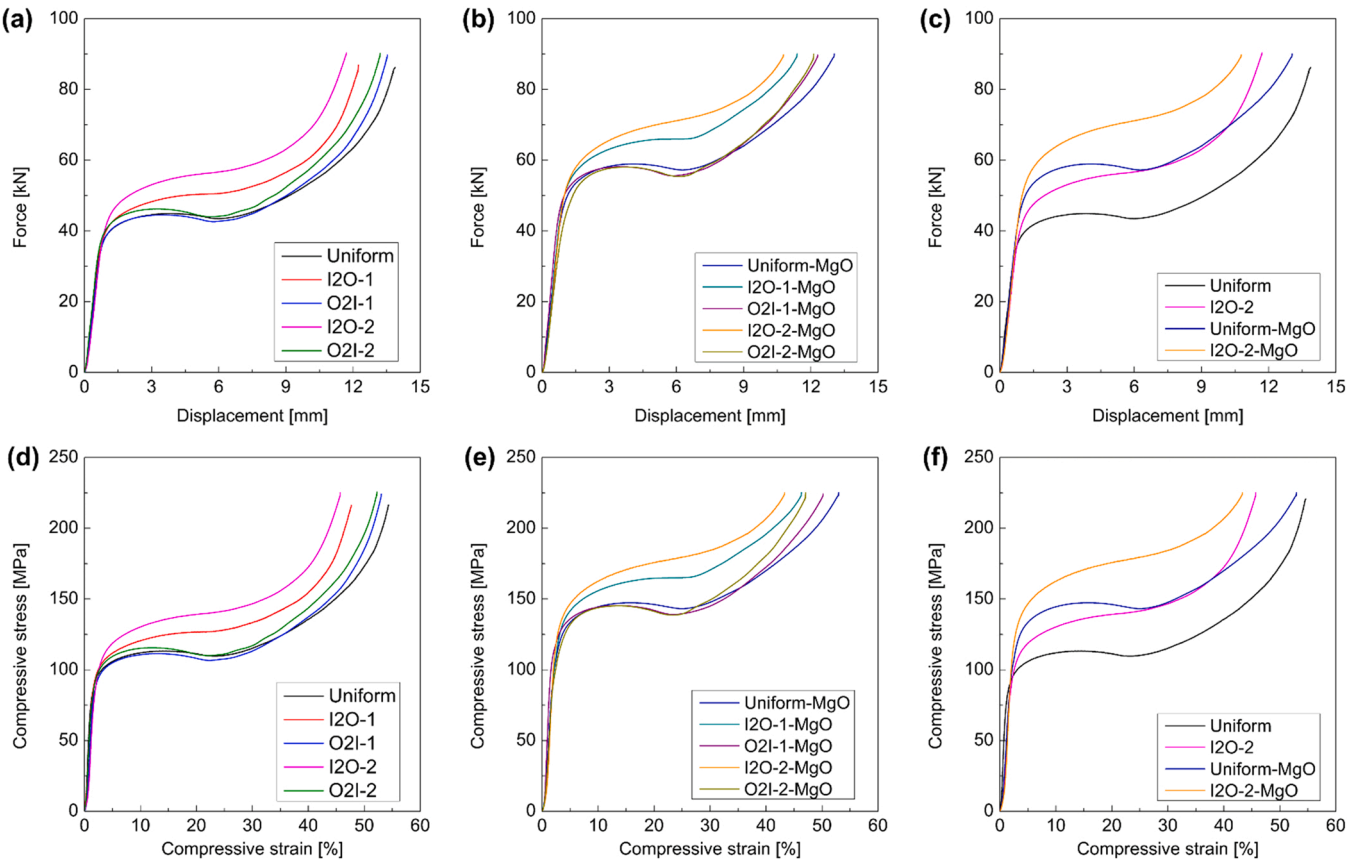

Fig. 10. The typical compressive stress–strain curves and the corresponding force–displacement curves of the lattice structures made from (a and d) CP−Ti, (b and e) MgO-doped CP−Ti, and (c and f) the comparison of the uniform and I2O-2 lattice structures without and with the addition of MgO.

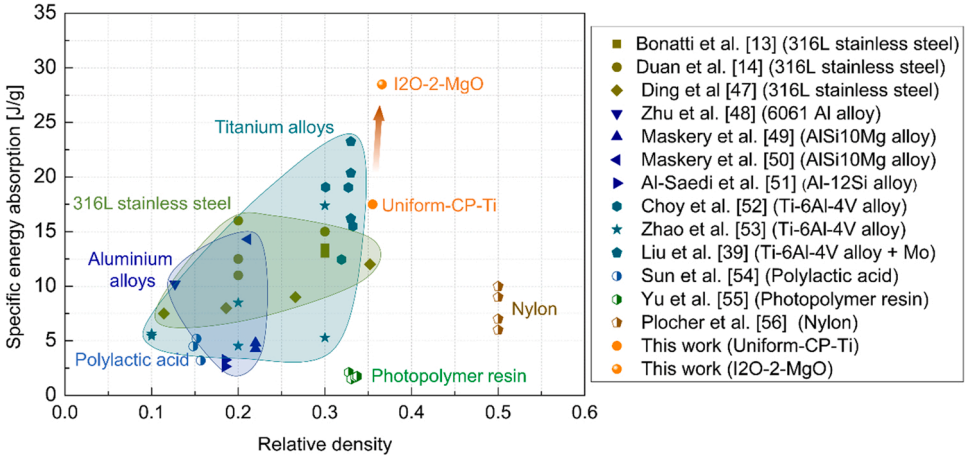

Fig. 11. Comparison of SEA of the lattice structures in this work with those reported in the literature.

this work, a modified VHM is used for FEA. Compared to the VHM, the following three main characteristic behaviours are captured in the modified VHM: (1) the tension-compression asymmetry of the struts, (2) the global anisotropic behaviour of the lattice structure itself, and (3) the influence of hydrostatic pressure on the mechanical response of material [36]. More details on the modified VHM and its applications to other lattice structures can be found in [36].

4.4.1. *Experimentally driven yield surface for gyroid lattice structures*

As schematically shown in Fig. 12, the original yield surface $F(p, \sigma_v)$ for the modified VHM is defined in terms of hydrostatic pressure (p) and von Mises stress (σ_v):

$$F(p, \sigma_v) = \sqrt{\sigma_v^2 + \alpha^2 (p - p_0)^2} - B = 0 \tag{7}$$

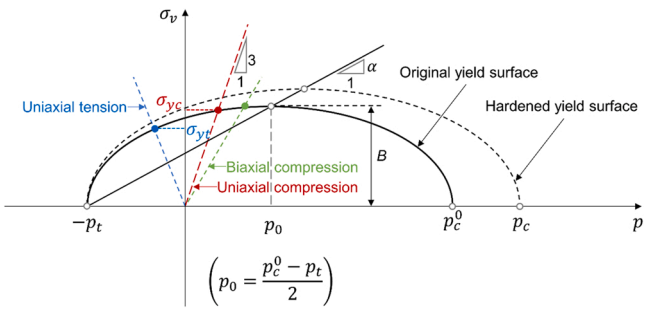

Fig. 12. The modified VHM yield surface used as a constitutive material model.

Table 4
The values for parameters in the Johnson-Cook damage model.

Parameter	D1	D2	D3	D4	D5	Displacement at failure
Value	0.05	0.15	1.2	0.002	0.46	0.2

where α is the is the shape factor of the yield ellipse:

$\alpha = \frac{3k}{\sqrt{(3k_t+k)(3-k)}}$

with.

$k = \frac{\sigma_{yc}}{p_c^0}$

and

$$k_t = \frac{p_t}{p_c^0} \tag{8}$$

$p_0$is the centre of the yield ellipse on the p-axis:

$$p_0 = \frac{p_c^0 - p_t}{2} \tag{9}$$

and B is the vertical size of the yield ellipse:

$$B = \alpha\left(\frac{p_c^0 + p_t}{2}\right) \tag{10}$$

In Eq. (8), σ_{yc} is the compressive yield strength, $p_c^0$and $p_t$are the yield strength in hydrostatic compression (the initial value of p_c) and the yield strength in hydrostatic tension, respectively. The evolution of yield surface is in a self-similar manner with constant shape factorα throughout the deformation process. As can be seen from Eqs. (7–10), p_c^0, $p_c$and $\sigma_{yc}$are unknowns. Therefore, with three unknowns, at least three different loading cases are required to plot the initial yield surface. In the present work, the experimentally obtained tensile yield strength and compressive yield strength (Supplementary Fig. S4), as well as the biaxial compression (from virtual laboratory approach [36]) are chosen as three different points (the blue, red and green dots as indicated in Fig. 12) to generate the original yield surface. Finally, a nonlinear least square method is employed to fit the initial yield surface using the yield point under the three different loading paths.

4.4.2. Numerical study on the deformation mechanisms of gyroid lattice structures

The deformation mechanisms of the uniform, I2O-2 and O2I-2 gyroid lattice structures under compressive loading were analysed based on the number of elements in tension (NET), the number of elements in compression (NEC), and the total number of the elements both in tension and compression (NET+NEC). If the volume of an element increases from increment n to increment $n + 1$, the considered element is under tensile loading in the $n + 1$ increment. The element with the volume change (i.e., ΔV) of zero or near zero indicates a non-zero deviatoric state of stress or that the element volume is changing less than 0.01%. Therefore, such elements were not considered in the calculation. A full description of this classification can be found in [36]. The number of failed elements (NFET) for each increment was also determined.

The dominant deformation and failure mechanisms that occurred in some key stages during compression (as marked with numbers on the compressive stress–strain curves) were studied in terms of the Johnson-Cook damage model. The Johnson-Cook damage model is defined by the strain for fracture, which is given by [35]:

$$\varepsilon^f = [D_1 + D_2 \exp D_3\sigma^*][1 + D_4 \ln \dot{\varepsilon}^*][1 + D_5 T^*] \tag{11}$$

where σ^* is the normalized flow stress and is defined as $\sigma^* = \sigma_m/\overline{\sigma}$ (where σ_m is hydrostatic pressure stress and $\overline{\sigma}$ is the von Mises equivalent stress). $\dot{\varepsilon}^* = \dot{\varepsilon}/\dot{\varepsilon}_0$ represents the normalized plastic strain rate for $\dot{\varepsilon}_0 = 1.0\ s^{-1}$. T^* is the normalized temperature and is defined as $T^* = (T - T_0)/(T_m - T_0)$ (here, T_0 is the reference temperature and T_m is the reference melt temperature). D_1, D_2, D_3, D_4 and D_5 are material-dependent damage constants. These constants were obtained by fitting the experimental results and are listed in Table 4. The Johnson-Cook damage initiation criterion (JCCRT) as a colour contour plot, in which damage initiates when the value is equal to or higher than unity, is used to investigate the facture behaviour inside the lattice structures. In-situ imaging of the deformation processes at various strain levels, which was recorded by a video camera, is provided to compare with the FEA.

For the uniform lattice structure as shown in Fig. 13, when the lattice structure starts yielding (Point 1), (NET+NEC) is around 90%, which indicates that 90% of the elements are involved in deformation, either under tension or under compression (Fig. 13a). With further straining up to Point 2, both NEC and (NET+NEC) tend to decrease while NET starts increasing. Between Point 1 and Point 3, the compressive stress–strain curve shows a hardening behaviour. Since the contact between struts has not yet taken place, this hardening behaviour is unlikely attributed to the structural response to compression, but mostly like results from the strain hardening of CP−Ti upon deformation. From Point 3 to Point 4, NEC decreases by almost 22% whereas NET increases by around 15%, resulting in a significant decrease of (NET+NEC). Besides, elements start to fail, and the number of failed elements increases sharply, as shown in Fig. 13b. The reduction in (NET+NEC) suggests that plastic strain localization takes place [36]. According to the JCCRT contour plot (Fig. 13c: 3 and 4 in the XZ-plane), the shear region at around 45° to the compression axis and the middle region exhibit higher JCCRT values and locally show the red colour, which confirms that strain localization occurs. In addition, in-situ images captured by the video camera also show the occurrence of shear bands (Fig. 13d: 4). This is consistent with other studies [21,58,59], which have reported that the occurrence of shear bands is responsible for the post-yielding softening or collapse behaviour.

The O2I-2 lattice structure exhibits a similar deformation behaviour to the uniform type (Fig. 14). When the lattice structure is strained from Point 3 to Point 4, (NET+NEC) decreases by about 10%, which is slightly higher than that of the uniform lattice structure. Similarly, the failure of element occurs in this strain range. From both JCCRT contour plots (Fig. 14c: 3 and 4 in the XZ-plane) and the in-situ imaging (Fig. 14d: 3 and 4), it can be observed that the shear and middle regions of the O2I-2 lattice structure becomes highly localized. As expected, the I2O-2 design is not capable of resisting the post-softening behaviour.

Unlike the uniform and O2I-2 lattice structures, the I2O-2 design does not show any post-yielding softening. It can be seen from Fig. 15a that after Point 3 NEC is decreasing while NET is increasing. This trend is similar to those in the uniform and O2I-2 lattice structures. However, (NET+NEC) remains almost constant and no failed element can be found when the strain level is less than 0.3 (Fig. 15b). This implies that the compressive loading is uniformly shared among all elements. The JCCRT contour plots confirm that a relatively homogeneous strain distribution across the I2O-2 lattice structure (Fig. 15c: 3–6). Additionally, in-situ imaging (Fig. 15d: 3) shows that the lattice sample is less strain localized compared with the uniform and I2O-2 lattice samples.

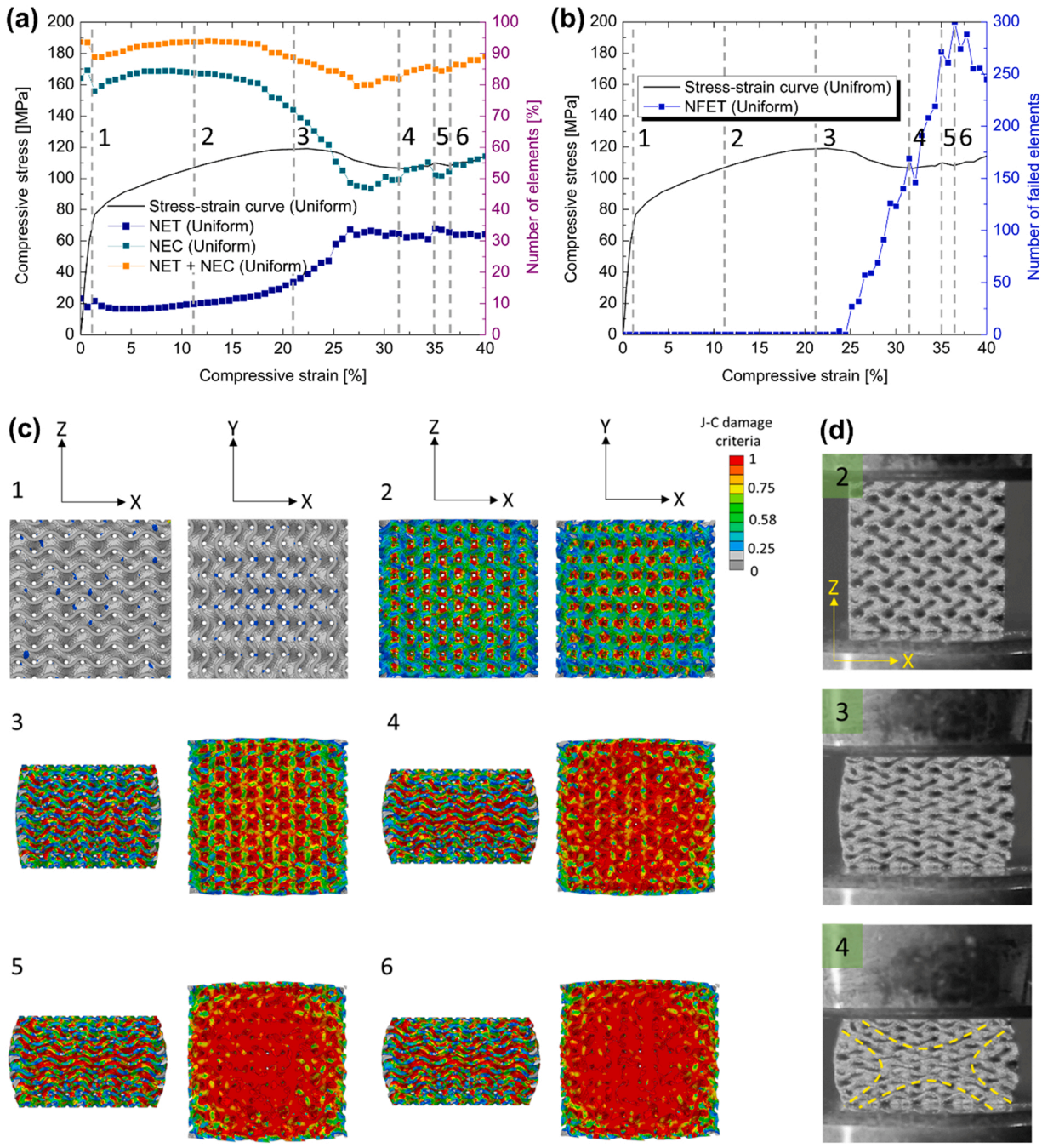

Fig. 13. FEA of the uniform lattice structure under compressive loading: (a) the NET, NEC, and (NET+NEC) are plotted against the compressive stress-strain curve, (b) the number of failed elements in each increment is plotted against the compressive stress-strain curve, (c) the Johnson-Cook contour plot during compression at the corresponding number points as marked in (a) or (b), and (d) the in-situ images captured by a video camera at various deformation stages.

From FEA, it can be found that deformation and failure initiate from the inner region in the lattice structures, regardless of the architectures (Fig. 13c: 1–4 in the XY-plane, Fig. 14c: 1–4 in the XY-plane and Fig. 15c: 1–4 in the XY-plane). In the I2O-2 design, the sheet thickness of the inner region is larger than those of the outer region. The higher relative density in the inner region enables the resistance of strain localization in the initial stage and the occurrence of shear band localization with further straining. Hence, this gives rise to the continuous hardening behaviour, rather than the post-yielding softening in the uniform and O2I-2 lattice structures.

It is noted that in this work the FEA was performed on the ideal lattice structures in view of simulation efficiency. Although the attached unmelted powders lead to an increase in the relative density (Fig. 5 and Table 1), it is shown that such attached powders do not neither significantly contribute to the strength [60], or act as the critical failure locations during deformation [61]. Besides, the manufacturing defects in the lattice structures used for FEA are kept at relatively low values (< 0.09%), as shown in Fig. 6a-c. Hence, the simulation results agree qualitatively well with the experimental results. Such a good agreement suggests that the modified VHM is capable of capturing the dominant characteristics that govern the deformation behaviour.

While the focus of this work is on improving the mechanical performance, the design and experimental work also directly endows the lattice structures with biological functions. Again, from the structural perspective, high strength and graded porosity of lattice structures are both required for long-term load-bearing bone implants. The I2O-2

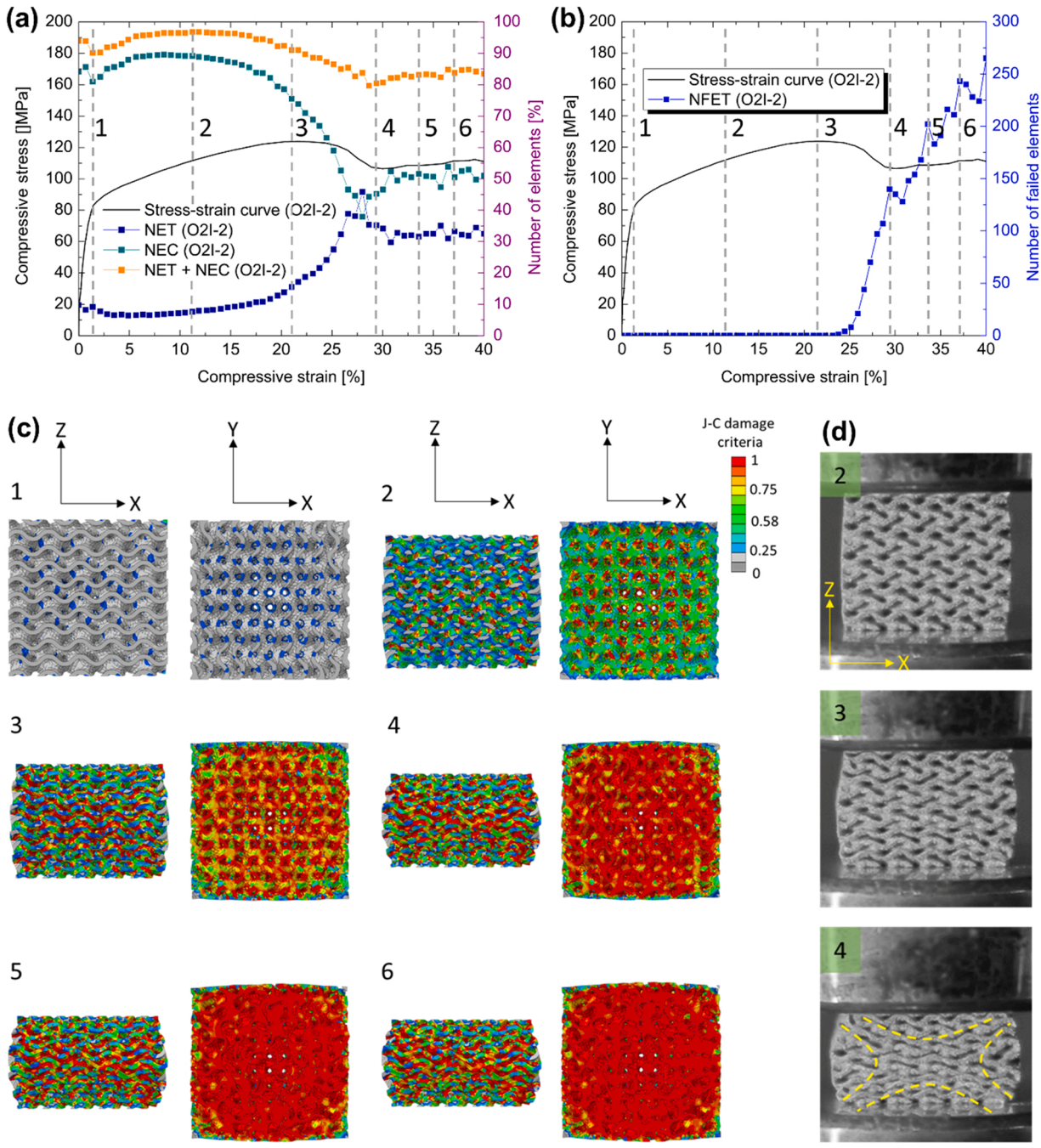

Fig. 14. FEA of the O2I-2 lattice structure under compressive loading: (a) the NET, NEC, and (NET+NEC) are plotted against the compressive stress-strain curve, (b) the number of failed elements in each increment is plotted against the compressive stress-strain curve, (c) the Johnson-Cook contour plot during compression at the corresponding number points as marked in (a) or (b), and (d) the in-situ images captured by a video camera at various deformation stages.

design shows higher strength compared with the uniform type. Additionally, the inner-to-outer pore gradient has been shown to enhance bone ingrowth [62]. From the material perspective, both CP−Ti and Ti−6Al−4V do not show the ideal material properties, either mechanical or biocompatible, for biomedical applications. CP−Ti shows excellent biocompatibility without toxic effects but exhibits inferior strength as compared with titanium alloys. In contrast, Ti−6Al−4V yields higher strength and fatigue resistance. However, the presence of Al and V might cause long-term health problems [17]. In this work, MgO nanoparticles were introduced to CP−Ti as the trace additive for enhancing the mechanical performance. It has been shown that MgO nanoparticles are biocompatible and even enable improving the integration of implanted biomaterials with bone [63,64]. Hence, the addition of MgO nanoparticles, whether melted or not during AM, does not introduce any adverse cytotoxicity. Additionally, compared with the biocompatible β-stabilizing elements such as Mo, Nb, and Ta, MgO is more cost-effective, making it attractive as the additive material to develop biomedical titanium lattice structures.

5. Conclusions

Gyroid lattice structures with uniform and graded sheet thickness were designed and fabricated via L-PBF from CP−Ti and MgO-doped CP−Ti feedstocks. The morphologies, microstructures and mechanical properties were investigated by means of SEM, Micro-CT, EBSD and compressive tests, respectively. The deformation behaviour and failure

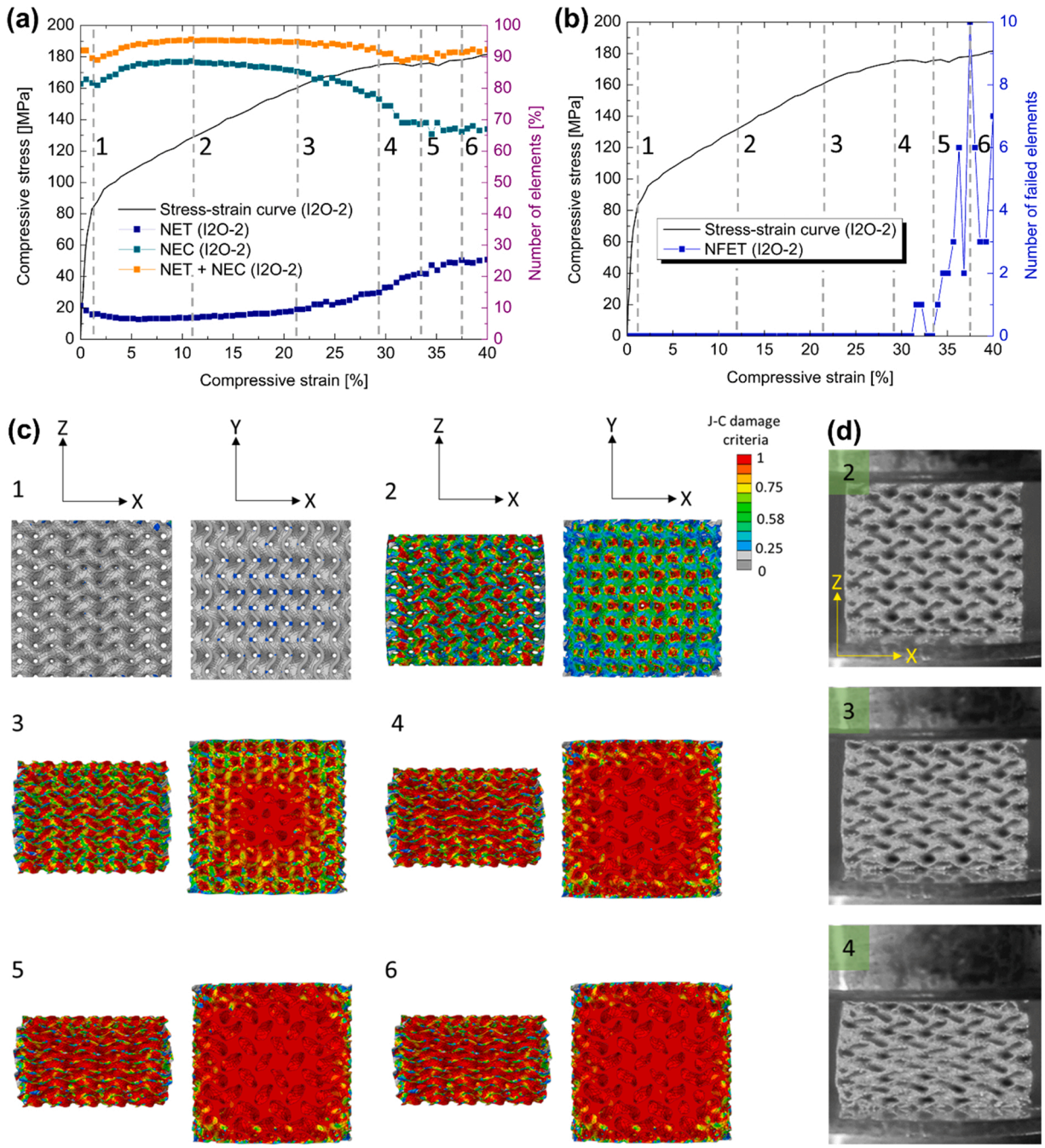

Fig. 15. FEA of the I2O-2 lattice structure under compressive loading: (a) the NET, NEC, and (NET+NEC) are plotted against the compressive stress-strain curve, (b) the number of failed elements in each increment is plotted against the compressive stress-strain curve, (c) the Johnson-Cook contour plot during compression at the corresponding number points as marked in (a) or (b), and (d) the in-situ images captured by a video camera at various deformation stages.

mode were studied by FEA which was based on the modified VHM. The following conclusions can be drawn from this work:

- Micro-CT characterizations show a small volume of manufacturing defects in the as-built samples. Either tailoring the sheet thickness gradient or adding MgO to CP−Ti does not considerably affect the manufacturing quality. Owing to the introduction of oxygen through MgO, the irregular shaped α phases of CP−Ti lattice structures transform into acicular α′ martensite in the MgO-doped types.
- Both the uniform and O2I lattice structures exhibit the typical post-yielding softening behaviour under compressive loading. The O2I designs result in negligible or even negative contribution to the strength enhancement compared to the uniform type. In contrast, the I2O designs show higher strength and a continuous hardening behaviour, with complete elimination of the post-yielding softening. The continuous hardening behaviour is intrinsic to the I2O designs and the addition of MgO does not change the deformation behaviour.
- The I2O-2 lattice structure made from MgO-doped feedstock shows superior SEA to the uniform CP−Ti type and outperforms most of metallic and polymeric lattice structures, due to the combination of high strength and the continuous strain hardening behaviour achieved through architecture engineering and material design.
- FEA results demonstrate that the I2O-2 lattice structures can resist the strain localization in the initial stage and the occurrence of shear band localization in the strain range, where post-yielding softening occurs in the uniform and O2I-2 lattice structures. FEA based on the

modified VHM could capture the features that govern the continuous hardening behaviour and shows good agreement with experimental results.

CRediT authorship contribution statement

Jingqi Zhang: Writing – review & editing, Writing – original draft, Validation, Methodology, Investigation, Data curation, Conceptualization. **Yingang Liu:** Writing – review & editing, Validation, Methodology, Investigation, Conceptualization. **Behzad Bahrami Babamiri:** Writing – review & editing, Methodology, Investigation. **Ying Zhou:** Writing – review & editing, Investigation. **Matthew Dargusch:** Writing – review & editing, Supervision. **Kavan Hazeli:** Writing – review & editing, Supervision, Conceptualization. **Ming-Xing Zhang**: Writing – review & editing, Supervision, Project administration, Conceptualization.

Declaration of Competing Interest

The authors declare that they have no known competing financial interests or personal relationships that could have appeared to influence the work reported in this paper.

Acknowledgments

J.Q. Zhang would like to thank the support of UQ Research Training Scholarships. The facilities and technical assistance of Australian Microscopy & Microanalysis Research Facility at the Centre for Microscopy and Microanalysis (CMM), The University of Queensland, are also acknowledged. M. Dargusch would like to acknowledge the support of the Australian Research Council through the ARC Research Hub for Advanced Manufacturing of Medical Devices (IH150100024). K. Hazeli would like to thank the Mechanics of Materials and Structures (MOMS) program at the National Science Foundation (NSF) under the Award Number: 1943465.

Appendix A. Supporting information

Supplementary data associated with this article can be found in the online version at doi:10.1016/j.addma.2022.102887.

References

[1] M.F. Ashby, The properties of foams and lattices, Philos. Trans. A. Math. Phys. Eng. Sci. 364 (2006) 15–30, https://doi.org/10.1098/rsta.2005.1678.
[2] A.G. Evans, J.W. Hutchinson, M.F. Ashby, Multifunctionality of cellular metal systems, Prog. Mater. Sci. 43 (1999) 171–221, https://doi.org/10.1016/S0079-6425(98)00004-8.
[3] Y.G. Liu, J.Q. Zhang, X.J. Gu, Y. Zhou, Y. Yin, Q.Y. Tan, M.Q. Li, M.-X. Zhang, Mechanical performance of a node reinforced body-centred cubic lattice structure manufactured via selective laser melting, Scr. Mater. 189 (2020) 95–100, https://doi.org/10.1016/j.scriptamat.2020.08.015.
[4] B.B. Babamiri, J.R. Mayeur, K. Hazeli, Synchronous involvement of topology and microstructure to design additively manufactured lattice structures, Addit. Manuf. 52 (2022), 102618, https://doi.org/10.1016/j.addma.2022.102618.
[5] R.R.J. Sélo, S. Catchpole-Smith, I. Maskery, I. Ashcroft, C. Tuck, On the thermal conductivity of AlSi10Mg and lattice structures made by laser powder bed fusion, Addit. Manuf. 34 (2020), 101214, https://doi.org/10.1016/j.addma.2020.101214.
[6] D. Carluccio, C. Xu, J. Venezuela, Y. Cao, D. Kent, M. Bermingham, A.G. Demir, B. Previtali, Q. Ye, M. Dargusch, Additively manufactured iron-manganese for biodegradable porous load-bearing bone scaffold applications, Acta Biomater. 103 (2020) 346–360, https://doi.org/10.1016/j.actbio.2019.12.018.
[7] T.A. Schaedler, A.J. Jacobsen, A. Torrents, A.E. Sorensen, J. Lian, J.R. Greer, L. Valdevit, W.B. Carter, Ultralight metallic microlattices, Science 334 (2011) 962–965, https://doi.org/10.1126/science.1211649.
[8] D. Jang, L.R. Meza, F. Greer, J.R. Greer, Fabrication and deformation of three-dimensional hollow ceramic nanostructures, Nat. Mater. 12 (2013) 893–898, https://doi.org/10.1038/nmat3738.
[9] X. Zheng, H. Lee, T.H. Weisgraber, M. Shusteff, J. DeOtte, E.B. Duoss, J.D. Kuntz, M.M. Biener, Q. Ge, J.A. Jackson, S.O. Kucheyev, N.X. Fang, C.M. Spadaccini, Ultralight, ultrastiff mechanical metamaterials, Science 344 (2014) 1373–1377, https://doi.org/10.1126/science.1252291.
[10] J. Berger, H. Wadley, R. McMeeking, Mechanical metamaterials at the theoretical limit of isotropic elastic stiffness, Nature 543 (2017) 533–537, https://doi.org/10.1038/nature21075.
[11] W. Chen, S. Watts, J.A. Jackson, W.L. Smith, D.A. Tortorelli, C.M. Spadaccini, Stiff isotropic lattices beyond the Maxwell criterion, Sci. Adv. 5 (2019), 1937, https://doi.org/10.1126/sciadv.aaw1937.
[12] T. Tancogne-Dejean, A.B. Spierings, D. Mohr, Additively-manufactured metallic micro-lattice materials for high specific energy absorption under static and dynamic loading, Acta Mater. 116 (2016) 14–28, https://doi.org/10.1016/j.actamat.2016.05.054.
[13] C. Bonatti, D. Mohr, Smooth-shell metamaterials of cubic symmetry: anisotropic elasticity, yield strength and specific energy absorption, Acta Mater. 164 (2019) 301–321, https://doi.org/10.1016/j.actamat.2018.10.034.
[14] S. Duan, W. Wen, D. Fang, Additively-manufactured anisotropic and isotropic 3D plate-lattice materials for enhanced mechanical performance: simulations & experiments, Acta Mater. 199 (2020) 397–412, https://doi.org/10.1016/j.actamat.2020.08.063.
[15] J. Bernal Ostos, R.G. Rinaldi, C.M. Hammetter, G.D. Stucky, F.W. Zok, A. J. Jacobsen, Deformation stabilization of lattice structures via foam addition, Acta Mater. 60 (2012) 6476–6485, https://doi.org/10.1016/j.actamat.2012.07.053.
[16] G.W. Kooistra, V.S. Deshpande, H.N.G. Wadley, Compressive behavior of age hardenable tetrahedral lattice truss structures made from aluminium, Acta Mater. 52 (2004) 4229–4237, https://doi.org/10.1016/j.actamat.2004.05.039.
[17] A. Ataee, Y. Li, B. Milan, C. Wen, Ultrahigh-strength titanium gyroid scaffolds manufactured by selective laser melting (SLM) for bone implant applications, Acta Mater. 158 (2018) 354–368, https://doi.org/10.1016/j.actamat.2018.08.005.
[18] L. Zhang, S. Feih, S. Daynes, S. Chang, M.Y. Wang, J. Wei, W.F. Lu, Energy absorption characteristics of metallic triply periodic minimal surface sheet structures under compressive loading, Addit. Manuf. 23 (2018) 505–515, https://doi.org/10.1016/j.addma.2018.08.007.
[19] L. Yang, C. Yan, W. Cao, Z. Liu, B. Song, S. Wen, C. Zhang, Y. Shi, S. Yang, Compression–compression fatigue behaviour of gyroid-type triply periodic minimal surface porous structures fabricated by selective laser melting, Acta Mater. 181 (2019) 49–66, https://doi.org/10.1016/j.actamat.2019.09.042.
[20] S.C. Kapfer, S.T. Hyde, K. Mecke, C.H. Arns, G.E. Schröder-Turk, Minimal surface scaffold designs for tissue engineering, Biomaterials 32 (2011) 6875–6882, https://doi.org/10.1016/j.biomaterials.2011.06.012.
[21] O. Al-Ketan, R. Rowshan, R.K.A. Al-Rub, Topology-mechanical property relationship of 3D printed strut, skeletal, and sheet based periodic metallic cellular materials, Addit. Manuf. 19 (2018) 167–183, https://doi.org/10.1016/j.addma.2017.12.006.
[22] I. Maskery, L. Sturm, A. Aremu, A. Panesar, C. Williams, C. Tuck, R.D. Wildman, I. Ashcroft, R.J. Hague, Insights into the mechanical properties of several triply periodic minimal surface lattice structures made by polymer additive manufacturing, Polymer 152 (2017) 62–71, https://doi.org/10.1016/j.polymer.2017.11.049.
[23] A. Issariyapat, S. Kariya, A. Alhazaa, J. Umeda, K. Kondoh, Additive manufacturing and characterization of high strength Ti-Zr gyroid scaffolds using pre-mixed Ti-ZrH_2 powders, JOM 73 (2021) 4166–4176, https://doi.org/10.1007/s11837-021-04923-4.
[24] M. Zhao, B. Ji, D.Z. Zhang, H. Li, H. Zhou, Design and mechanical performances of a novel functionally graded sheet-based lattice structure, Article 102676, Addit. Manuf. 52 (2022), https://doi.org/10.1016/j.addma.2022.102676.
[25] A. Alhammadi, O. Al-Ketan, K.A. Khan, M. Ali, R. Rowshan, R.K.Abu Al-Rub, Microstructural characterization and thermomechanical behavior of additively manufactured AlSi10Mg sheet cellular materials, Mater. Sci. Eng., A 791 (2020), 139714, https://doi.org/10.1016/j.msea.2020.139714.
[26] L. Yang, R. Mertens, M. Ferrucci, C. Yan, Y. Shi, S. Yang, Continuous graded gyroid cellular structures fabricated by selective laser melting: design, manufacturing and mechanical properties, Mater. Des. 162 (2019) 394–404, https://doi.org/10.1016/j.matdes.2018.12.007.
[27] D. Li, W. Liao, N. Dai, Y.M. Xie, Comparison of mechanical properties and energy absorption of sheet-based and strut-based gyroid cellular structures with graded densities, Materials 12 (13) (2019), 2183, https://doi.org/10.3390/ma12132183.
[28] D. Mahmoud, K.S. Al-Rubaie, M.A. Elbestawi, The influence of selective laser melting defects on the fatigue properties of Ti6Al4V porosity graded gyroids for bone implants, Int. J. Mech. Sci. 193 (2021), 106180, https://doi.org/10.1016/j.ijmecsci.2020.106180.
[29] L. Yang, S. Wu, C. Yan, P. Chen, L. Zhang, C. Han, C. Cai, S. Wen, Y. Zhou, Y. Shi, Fatigue properties of Ti-6Al-4V Gyroid graded lattice structures fabricated by laser powder bed fusion with lateral loading, Addit. Manuf. 46 (2021), 102214, https://doi.org/10.1016/j.addma.2021.102214.
[30] M.H. Mosallanejad, B. Niroumand, A. Aversa, A. Saboori, In-situ alloying in laser-based additive manufacturing processes: a critical review, J. Alloy. Compd. 872 (2021), 159567, https://doi.org/10.1016/j.jallcom.2021.159567.
[31] N. Soro, H. Attar, E. Brodie, M. Veidt, A. Molotnikov, M.S. Dargusch, Evaluation of the mechanical compatibility of additively manufactured porous Ti–25Ta alloy for load-bearing implant applications, J. Mech. Behav. Biomed. Mater. 97 (2019) 149–158, https://doi.org/10.1016/j.jmbbm.2019.05.019.
[32] M.H. Mosallanejad, B. Niroumand, A. Aversa, D. Manfredi, A. Saboori, Laser powder bed fusion in-situ alloying of Ti–5%Cu alloy: process-structure relationships, J. Alloy. Compd. 857 (2021), 157558, https://doi.org/10.1016/j.jallcom.2020.157558.
[33] D.W. Wang, Y.H. Zhou, J. Shen, Y. Liu, D.F. Li, Q. Zhou, G. Sha, P. Xu, T. Ebel, M. Yan, Selective laser melting under the reactive atmosphere: a convenient and Efficient approach to fabricate ultrahigh strength commercially pure titanium

without sacrificing ductility, Mater. Sci. Eng. A 762 (2019), 138078, https://doi.org/10.1016/j.msea.2019.138078.
[34] ISO 13314, Mechanical testing of metals–ductility, Testing–Compression Test for Porous and Cellular Metals (2011) 1–7.
[35] G.R. Johnson, W.H. Cook, Fracture characteristics of three metals subjected to various strains, strain rates, temperatures and pressures, Eng. Fract. Mech. 21 (1985) 31–48, https://doi.org/10.1016/0013-7944(85)90052-9.
[36] B.B. Babamiri, H. Askari, K. Hazeli, Deformation mechanisms and post-yielding behavior of additively manufactured lattice structures, Mater. Des. 188 (2020), 108443, https://doi.org/10.1016/j.matdes.2019.108443.
[37] X.P. Li, G. Ji, K. Eder, L.M. Yang, A. Addad, J. Vleugels, J. Van Humbeeck, J. M. Cairney, J.P. Kruth, Additive manufacturing of a novel alpha titanium alloy from commercially pure titanium with minor addition of Mo_2C, Materialia 4 (2018) 227–236, https://doi.org/10.1016/j.mtla.2018.09.033.
[38] M. Janecek, Reflectivity spectra for commonly used reflectors, IEEE Trans. Nucl. Sci. 59 (2012) 490–497, https://doi.org/10.1109/TNS.2012.2183385.
[39] Y.G. Liu, J.Q. Zhang, Q.T. Tan, Y. Yin, M.Q. Li, M.-X. Zhang, Mechanical performance of simple cubic architected titanium alloys fabricated via selective laser melting, Opt. Laser Technol. 134 (2021), 106649, https://doi.org/10.1016/j.optlastec.2020.106649.
[40] M. Yan, W. Xu, M.S. Dargusch, H.P. Tang, M. Brandt, M. Qian, Review of effect of oxygen on room temperature ductility of titanium and titanium alloys, Powder Metall. 57 (2014) 251–257, https://doi.org/10.1179/1743290114Y.0000000108.
[41] H.J.T. Ellingham, Reducibility of oxides and sulfides in metallurgical processes, J. Soc. Chem. Ind. 63 (1944) 125–133, https://doi.org/10.1002/jctb.5000630501.
[42] University of Cambridge. Dissemination of IT for the Promotion of Materials Science (DoITPoMS). ⟨https://www.doitpoms.ac.uk/tlplib/ellingham_diagrams/ellingham.php⟩, 2022. (accessed 14 February 2022).
[43] J.Q. Zhang, Y.G. Liu, M. Bayat, Q.Y. Tan, Y. Yin, Z.Q. Fan, S.Y. Liu, J.H. Hattel, M. Dargusch, M.-X. Zhang, Achieving high ductility in a selectively laser melted commercial pure-titanium via in-situ grain refinement, Scr. Mater. 191 (2021) 155–160, https://doi.org/10.1016/j.scriptamat.2020.09.023.
[44] P.A. Hooper, Melt pool temperature and cooling rates in laser powder bed fusion, Addit. Manuf. 22 (2018) 548–559, https://doi.org/10.1016/j.addma.2018.05.032.
[45] J. Liu, C. Suryanarayana, D. Ghosh, G. Subhash, L. An, Synthesis of Mg-Al_2O_3 nanocomposites by mechanical alloying, J. Alloy. Compd. 563 (2013) 165–170, https://doi.org/10.1016/j.jallcom.2013.01.113.
[46] K. Grjotheim, O. Herstad, J.M. Toguri, The aluminum reduction of magnesium oxide: I. The vapor pressure of magnesium over the system Al-MgO, Can. J. Chem. 39 (1961) 443–450, https://doi.org/10.1139/v61-05.
[47] R. Ding, J. Yao, B. Du, L. Zhao, Y. Guo, Mechanical properties and energy absorption capability of ARCH lattice structures manufactured by selective laser melting, Adv. Eng. Mater. 22 (2020), 1901534, https://doi.org/10.1002/adem.201901534.
[48] Y. Zhu, Z.-P. Wang, L.H. Poh, Auxetic hexachiral structures with wavy ligaments for large elasto-plastic deformation, Smart Mater. Struct. 27 (2018), 055001, https://doi.org/10.1088/1361-665X/aab33d.
[49] I. Maskery, N.T. Aboulkhair, A.O. Aremu, C.J. Tuck, I.A. Ashcroft, R.D. Wildman, R.J.M. Hague, A mechanical property evaluation of graded density Al-Si10-Mg lattice structures manufactured by selective laser melting, Mater. Sci. Eng. A 670 (2016) 264–274, https://doi.org/10.1016/j.msea.2016.06.013.
[50] I. Maskery, N.T. Aboulkhair, A. Aremu, C. Tuck, I. Ashcroft, Compressive failure modes and energy absorption in additively manufactured double gyroid lattices, Addit. Manuf. 16 (2017) 24–29, https://doi.org/10.1016/j.addma.2017.04.003.
[51] D.S.J. Al-Saedi, S.H. Masood, M. Faizan-Ur-Rab, A. Alomarah, P. Ponnusamy, Mechanical properties and energy absorption capability of functionally graded F2BCC lattice fabricated by SLM, Mater. Des. 144 (2018) 32–44, https://doi.org/10.1016/j.matdes.2018.01.059.
[52] S.Y. Choy, C.-N. Sun, K.F. Leong, J. Wei, Compressive properties of functionally graded lattice structures manufactured by selective laser melting, Mater. Des. 131 (2017) 112–120, https://doi.org/10.1016/j.matdes.2017.06.006.
[53] M. Zhao, F. Liu, G. Fu, D. Zhang, T. Zhang, H. Zhou, Improved mechanical properties and energy absorption of BCC lattice structures with triply periodic minimal surfaces fabricated by SLM, Materials 11 (2018), 2411, https://doi.org/10.3390/ma11122411.
[54] Z.P. Sun, Y.B. Guo, V.P.W. Shim, Characterisation and modeling of additively-manufactured polymeric hybrid lattice structures for energy absorption, Int. J. Mech. Sci. 191 (2021), 106101, https://doi.org/10.1016/j.ijmecsci.2020.106101.
[55] S. Yu, J. Sun, J. Bai, Investigation of functionally graded TPMS structures fabricated by additive manufacturing, Mater. Des. 182 (2019), 08021, https://doi.org/10.1016/j.matdes.2019.108021.
[56] J. Plocher, A. Panesar, Effect of density and unit cell size grading on the stiffness and energy absorption of short fibre-reinforced functionally graded lattice structures, Article 101171, Addit. Manuf. 33 (2020), https://doi.org/10.1016/j.addma.2020.101171.
[57] V. Deshpande, N. Fleck, Isotropic constitutive models for metallic foams, J. Mech. Phys. Solids 48 (6–7) (2000) 1253–1283, https://doi.org/10.1016/S0022-5096(99)00082-4.
[58] M.-S. Pham, C. Liu, I. Todd, J. Lertthanasarn, Damage-tolerant architected materials inspired by crystal microstructure, Nature 565 (2019) 305–311, https://doi.org/10.1038/s41586-018-0850-3.
[59] C. Qiu, S. Yue, N.J.E. Adkins, M. Ward, H. Hassanin, P.D. Lee, P.J. Withers, M. M. Attallah, Influence of processing conditions on strut structure and compressive properties of cellular lattice structures fabricated by selective laser melting, Mater. Sci. Eng.: A 628 (2015) 188–197, https://doi.org/10.1016/j.msea.2015.01.031.
[60] T. Maconachie, M. Leary, B. Lozanovski, X. Zhang, M. Qian, O. Faruque, M. Brandt SLM lattice structures: properties, performance, applications and challenges, Mater. Des. (2019), Article 108137. ⟨https://doi.org/10.1016/j.matdes.2019.108137⟩.
[61] A. Jam, A. du Plessis, C. Lora, S. Raghavendra, M. Pellizzari, M. Benedetti, Manufacturability of lattice structures fabricated by laser powder bed fusion: a novel biomedical application of the beta Ti-21S alloy, Addit. Manuf. 50 (2022), 102566, https://doi.org/10.1016/j.addma.2021.102556.
[62] D. Barba, E. Alabort, R.C. Reed, Synthetic bone: design by additive manufacturing, Acta Biomater. 97 (2019) 637–656, https://doi.org/10.1016/j.actbio.2019.07.049.
[63] F. Khorashadizade, S. Abazari, M. Rajabi, H.R. Bakhsheshi-Rad, Ahmad Fauzi Ismail, Safian Sharif, Seeram Ramakrishna, F. Berto, Overview of magnesium-ceramic composites: mechanical, corrosion and biological properties, J. Mater. Res. Technol. 15 (2021) 6034–6066, https://doi.org/10.1016/j.jmrt.2021.10.141.
[64] S.Z. Khalajabadi, M.R. Abdul Kadir, S. Izman, R. Ebrahimi-Kahrizsangi, Fabrication, bio-corrosion behavior and mechanical properties of a Mg/HA/MgO nanocomposite for biomedical applications, Mater. Des. 88 (2015) 1223–1233, https://doi.org/10.1016/j.matdes.2015.09.065.